Research Activities

– Synchrotron Radiation Experiments –

Angle-Resolved Photoemission Study of Hybridization Effect in $YbInCu_4$

S. Ishihara[a], K. Ichiki[a], K. Abe[a], T. Matsumoto[a], K. Mimura[a,b], H. Sato[b], M. Arita[b], Eike F. Schwier[b], H. Iwasawa[b], K. Shimada[b], H. Namatame[b], M. Taniguchi[b], T. Zhuang[c], K. Hiraoka[c], and H. Anzai[a]

[a] *Graduate School of Engineering, Osaka Prefecture University, Sakai 599-8531, Japan*
[b] *Hiroshima Synchrotron Radiation Center (HSRC), Hiroshima University, Higashi-Hiroshima 739-0046, Japan*
[c] *Graduate School of Science and Engineering, Ehime University, Matsuyama 790-8577, Japan*

Keywords: Valence transition, Yb compound, angle-resolved photoemission spectroscopy.

In rare-earth compounds, the hybridization between conduction and localized-*f* electrons (*c-f* hybridization) has been one of the most intriguing subjects. In particular, $YbInCu_4$ has attracted great interests for a long time, because it exhibits a first-order valence transition at T_v = 42 K and concomitantly changes Kondo temperature, which is a measure of the *c-f* hybridization strength, from T_K ~ 25 K in high-temperature phase to T_K ~ 400 K in low-temperature phase [1,2]. Hence, the valence transition of $YbInCu_4$ is closely related to the *c-f* hybridization. Photoemission spectroscopy is an excellent tool for quantifying the valence from spectral intensities and has been known to provide direct insight into the valence transition [3,4]. However, the details of momentum-resolved electronic structure of $YbInCu_4$ remain unclear. In the periodic Anderson model, the *c-f* hybridization opens an energy gap at the crossing point of the conduction and *f* bands, and forms two energy branches (E_k^+ and E_k^-). E_k^+ and E_k^- are described by

$$E_k^{\pm} = \frac{1}{2}\left\{\varepsilon_f + \varepsilon_c \pm \sqrt{(\varepsilon_f - \varepsilon_c)^2 + 4V_{eff}{}^2}\right\}, \quad (1)$$

where ε_c and ε_f are conduction-band and *f*-band energies, respectively. The magnitude of the gap energy depends on the value of V_{eff}. To reveal the hybridization effect directly, the momentum resolved data are indispensable. Here, we report an angle-resolved photoemission spectroscopy (ARPES) study on single crystalline $YbInCu_4$ using synchrotron radiation. For the first time, we have observed the band dispersions near the Fermi energy (E_F) and revealed a bending of the flat band at $|\omega|$ ~ 0.15 eV. On the basis of a comparison with the periodic Anderson model, we show that the band bending is derived from the *c-f* hybridization effect. The ARPES measurements were performed at BL-1 of Hiroshima Synchrotron Radiation Center. Total energy resolution was set to 20 meV. The samples were cleaved *in situ* along the (111) crystal plane and collected at 19 K in a vacuum better than 2.6×10^{-10} Torr. The excitation photon energy was $h\nu$ = 50 eV.

Figure 1(a) shows ARPES spectra taken along a momentum cut slightly off the Γ-K direction. Two flat bands are clearly visible at $|\omega|$ ~ 0.05 and 1.35 eV. We respectively assigned these two bands to the bulk-derived Yb^{+2} $4f_{7/2}$ and $4f_{5/2}$ states. Furthermore, there exists a surface-derived Yb^{+2} contribution around $|\omega|$ ~ 1.0 eV, which originates from reduced *c-f* hybridization near the surface [5]. The widely dispersive bands are clearly observed over an energy range of $0.5 < |\omega| < 1.5$ eV. These bands can be attributed to the In 5*p* states by comparing with band calculation [6]. We found that a weak flat band at $|\omega|$ ~ 0.15 eV below the bulk Yb^{+2} $4f_{7/2}$ state is curved around k ~ 0.8 Å^{-1}. The result suggests an existence of the *c-f* hybridized energy bands. For in-depth analysis, the band dispersion is fitted with a model function (1), and the result is overlaid as black curves in Fig. 1(b). The lower energy branch well captures the curved band distribution. The hybridization energy V_{eff} is estimated as 35 meV, which is comparable with T_K ~ 400 K in the low-temperature phase. It should be noted that the flat band at $|\omega|$ ~ 0.15 eV is different from the multiplet terms of the bulk Yb $4f^{13}$ final state because the splitting energy of 0.1 eV is ten times larger than the prediction from neutron scattering experiments [7].

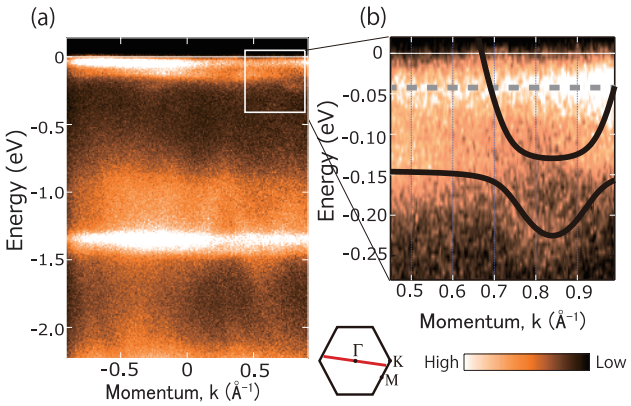

Figure 1. (a) ARPES spectra of $YbInCu_4$ taken at $T = 19$ K with $h\nu = 50$ eV. (b) Band dispersions over a field of view marked by white square in (a). Black curves and dashed line show the results of fitting using model function (1) and the energy position of the bulk Yb^{+2} $4f_{7/2}$ state, respectively.

We assigned the flat band at $|\omega| \sim 0.15$ eV as the Yb^{+2} $4f_{7/2}$ states derived from the Yb atom in sub-surface region of the $YbInCu_4$ crystals, which is likely to be the second or third Yb layers from the surface [4]. We assume that the electronic structure in the sub-surface region should have intermediate characters between those at surface and in the bulk. Indeed, the well-defined peak at $|\omega| \sim 0.15$ eV is located in between the surface-derived state at $|\omega| \sim 1$ eV and bulk-derived state at $|\omega| \sim 0.05$ eV. Therefore, the observed band bending is evidence for the hybridization effect between the conduction and sub-surface-derived $4f$ states.

In summary, we report angle-resolved photoemission spectroscopy measurements on the first-order valence-transition compound $YbInCu_4$. For the first time, we observed a flat band at ~ 0.15 eV below the bulk Yb^{+2} $4f_{7/2}$ states together with a sudden change of the dispersion curvature, which is consistent with the hybridization-band picture based on the periodic Anderson model. The estimated hybridization energy of 35 meV is comparable to the Kondo temperature in the low-temperature phase. We attributed the flat band to the localized $4f$ states derived from the Yb atom in the sub-surface region of $YbInCu_4$.

References

[1] I. Felner *et al*., Phys. Rev. B **35**, 6956 (1987).
[2] J. L. Sarrao, C. D. Immer, C. L. Benton, and Z. Fisk, Phy. Rev. B **54**, 12208 (1996).
[3] H. Sato *et al*., Phy. Rev. Lett. **93**, 246404 (2004).
[4] S. Suga *et al*., J. Phys. Soc. Jpn. **78**, 074704 (2009).
[5] F. Reinert *et al*., Phys. Rev. B **58**, 12808 (1998).
[6] V. N. Antonov, M. Galli, and F. Marabelli, Phys. Rev. B **62**, 1746 (2000).
[7] G. Polatsek, and P. Bonville, Phys. B **88**, 189 (1992).

Multi-band electronic structure of $Eu_3F_4Bi_2S_4$

T. Mizokawa[a], T. Sugimoto[b], E. Paris[d], N. L. Saini[d],
T. Asano[e], H. Endo[e], M. Mita[e], R. Higashinaka[e], T. Matsuda[e], Y. Aoki[e],
E. F. Schwier[f], M. Zheng[f], K. Kojima[f], H. Iwasawa[f],
K. Shimada[f], H. Namatame[f], M. Taniguchi[f,g]

[a] *Department of Applied Physics, Waseda University, Shinjuku-ku, Tokyo 169-8555, Japan*
[b] *Department of Complexity Science and Engineering, University of Tokyo, Kashiwa, Chiba 277-8561, Japan*
[c] *Department of Physics, University of Tokyo, Kashiwa, Chiba 277-8561, Japan*
[d] *Department of Physics, University of Roma "La Sapienza", Piazzale Aldo Moro 2, 00185 Roma, Italy*
[e] *Department of Physics, Tokyo Metropolitan University, Hachioji, Tokyo 192-0397, Japan*
[f] *HiSOR, Hiroshima University, Higashihiroshima, Hiroshima 739-0046, Japan*
[g] *Graduate School of Science, Hiroshima University, Higashihiroshima, Hiroshima 739-8526, Japan*

Keywords: Kondo physics, Eu 4*d*-4*f* resonance, BiS_2 superconductor

Since the discovery of superconductivity in the BiS_2 system by Mizuguchi *et al.* [1], the electronic structures of the BiS_2-based superconductors have been studied extensively by means of various spectroscopic methods. In most of the BiS_2-based compounds including $CeO_{1-x}F_xBiS_2$, superconductivity can be induced by introducing carriers in the BiS_2 plane by chemical substitution. The title system $Eu_3F_4Bi_2S_4$ is quite unique in that the BiS_2 plane is already superconducting without chemical substitution due to the valence instability of Eu [2]. As for angle-resolved photoemission spectroscopy (ARPES) studies on the BiS_2-based compounds, the Fermi pockets around X point of the Brillouin zone are reported and are identified as the Bi $6p_x/6p_y$ orbitals that are responsible for the superconductivity [3-5]. In order to examine the contribution of the Eu 4*f* states to the valence band near the Fermi level, we have performed Eu 4*d*-4*f* resonant angle-resolved photoemission spectroscopy on $Eu_3F_4Bi_2S_4$ at BL-1, HiSOR.

The left and right panels of Fig. 1 show the ARPES data taken at 134eV (off-resonance) and 140 eV (on-resonance), respectively, for $Eu_3F_4Bi_2S_4$. The momentum is running along the Γ-X direction of the Brillouin zone. The Fermi pockets around X point (constructed from the Bi 6*p* orbitals) are not clearly observed in the off-resonance data although they are observed at lower photon energies. The valence bands below 1 eV can be assigned to Bi 6*s*, S 3*p*, and Eu 4*f* bands. When the photon energy is tuned to the Eu 4*d*-4*f* absorption energy (140 eV), the flat band located around 2 eV is enhanced indicating that the Eu 4*f* electrons are basically localized and do not contribute to the Fermi pockets around X. The energy distribution curve for the on-resonance photon energy exhibits an intense Ce 4*f* peak at -1.5 eV. The resonant ARPES results show that the Eu 4*f* band is located between the Bi 6*p* conduction band and the Bi 6*s*/S 3*p* valence band, and that there is no appreciable Eu 4*f* spectral weight at the Fermi level.

REFERENCES

1. Y. Mizuguchi, H. Fujihisa, Y. Gotoh, K. Suzuki, H. Usui, K. Kuroki, S. Demura, Y. Takano, H. Izawa, and O. Miura, Phys. Rev. B **86**, 220510(R) (2012).
2. H.-F. Zhai, P. Zhang, S.-Q. Wu, C.-Y. He, Z.-T. Tang, H. Jiang, Y.-L. Sun, J.-K. Bao, I. Nowik, I. Felner, Y.-W. Zeng, Y.-K. Li, X.-F. Xu, Q. Tao, Z.-A. Xu, and G.-H. Cao *et al.*, J. Am. Chem. Soc. **136**, 15386 (2014).
3. Z. R. Ye, H. F. Yang, D. W. Shen, J. Jiang, X. H. Niu, D. L. Feng, Y. P. Du, X. G. Wan, J. Z. Liu, X. Y. Zhu, H. H. Wen, and M. H. Jiang, Phys. Rev. B **90**, 045116 (2014).
4. L. K. Zeng, X. B. Wang, J. Ma, P. Richard, S. M. Nie, H. M. Weng, N. L. Wang, Z. Wang, T. Qian, and H. Ding, Phys. Rev. B **90**, 054512 (2014).
5. N. L. Saini, D. Ootsuki, E. Paris, B. Joseph, A. Barinov, M. Tanaka, Y. Takano, and T. Mizokawa, Phys. Rev. B **90**, 214517 (2014).

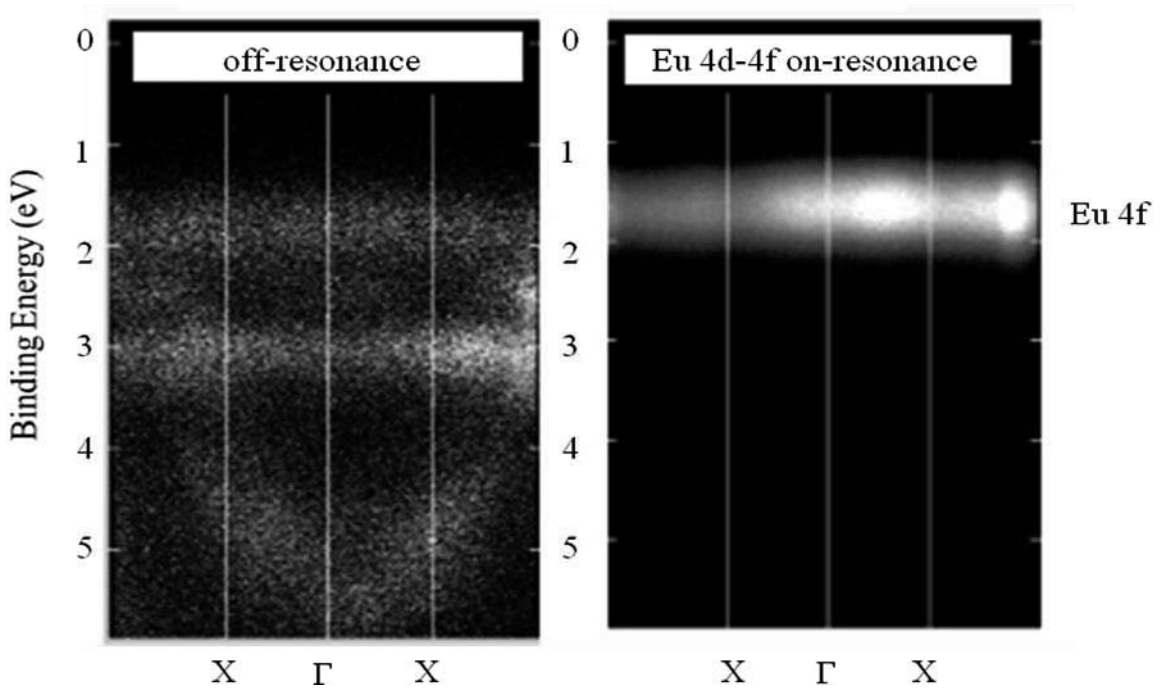

FIGURE 1. Right panel: ARPES spectra of $Eu_3F_4Bi_2S_4$ along the Γ-X direction taken at 134 eV (off-resonance). Left panel: ARPES spectra of $Eu_3F_4Bi_2S_4$ along the Γ-X direction taken at 140 eV (on-resonance).

Spiral structure in the intensity distribution of the photoelectron emission from the Dirac cone of graphene

Shin-ichiro Tanaka[a]

[a] *The Institute of Scientific and Industrial Research, Osaka University*

Keywords: ARPES, graphene, SiC, Dirac cone, phase

The Dirac cone formed by the π-band of graphene exhibits a linear dispersion as a function of the electron momentum. The wavefunction of the Dirac cone is described by a simple formula including the phase term of $\exp(i\theta_q)$, where θ_q is the angle around the K-point in the reciprocal lattice space.[1] Therefore, graphene is one of the simplest and most suitable systems for studying a problem concerning the phase of the wavefunction in condensed matter physics, e.g., the Berry's phase. From this point of view, a number of the angle-resolved photoelectron spectroscopy (ARPES) studies were carried out to investigate the photoelectron intensity distribution depending on linear and circular polarizations of the incident photons.[1] Recently, we measured the intensity distribution near the Fermi edge of the Dirac cone along the Γ-K-M line as a function of both the photon energy and the linear polarization angle, and compared it to the theoretical calculation [2]. It was proposed that the photoelectron intensity is determined by the matrix element $\langle \varphi_f | H_{opt} | \varphi_i \rangle$, which is the product of the initial and final states and the operator for the optical transition. The strong photon-energy dependence in the intensity distribution indicates that the final state can not be regarded as the plane wave which does not change its character with changing the binding energy. The symmetric properties of unocc;uied bads of graphene varies as a function of the binding energy, which in turn may cause the strong photon-energy dependence. We found that the intensity distribution at the Fermi level along the Γ-K-M line changes drastically near the photon energy of 45eV. Therefore, we can expect the drastic change in the intensity distribution within the ARPES spectrum as a function of the binding energy when it is taken at a photon energy of about 45eV, because the final state changes as a function of the binding energy.

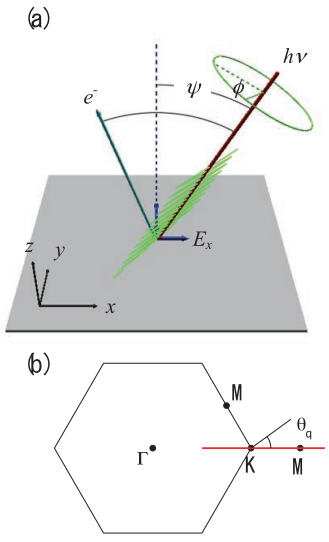

Fig.1 : Experimental geometry for the ARPES measurements and the definition of the phase θ_q.

The experiments were carried out at the HiSOR BL-1, where the polarization angle can be varied at any value from the s-pol to p-pol by rotating the analyzer chamber equipped with the electron analyzer. The single-layered epitaxial graphene on SiC substrate was used and the temperature during the measurement was 30K. Fig. 1(a) shows the experimental geometry, and Fig. 1(b) shows the measured Dirac cone hereafter and the definition of the phase θ_q.

Figures 2 show the intensity distribution maps in the k_x-k_y plane of the Dirac cone measured with the ARPES taken at 47eV. The maps at the binding energies of "-0.1" eV correspond to the maps at the Fermi level, and those of "-0.41" eV to those at the Dirac point. Figs 2(a) is taken at the polarization angle $\phi=0^o$, which correspond to p-polarization, and Figs. 2(b) are taken at $\phi=80^o$, which is close to s-polarization, but including a non-negligible p-polarized component. In both cases, similar Fermi surfaces are observed, and circles are distorted to three-hold symmetric away from the Dirac point. However, the intensity distribution is completely different as

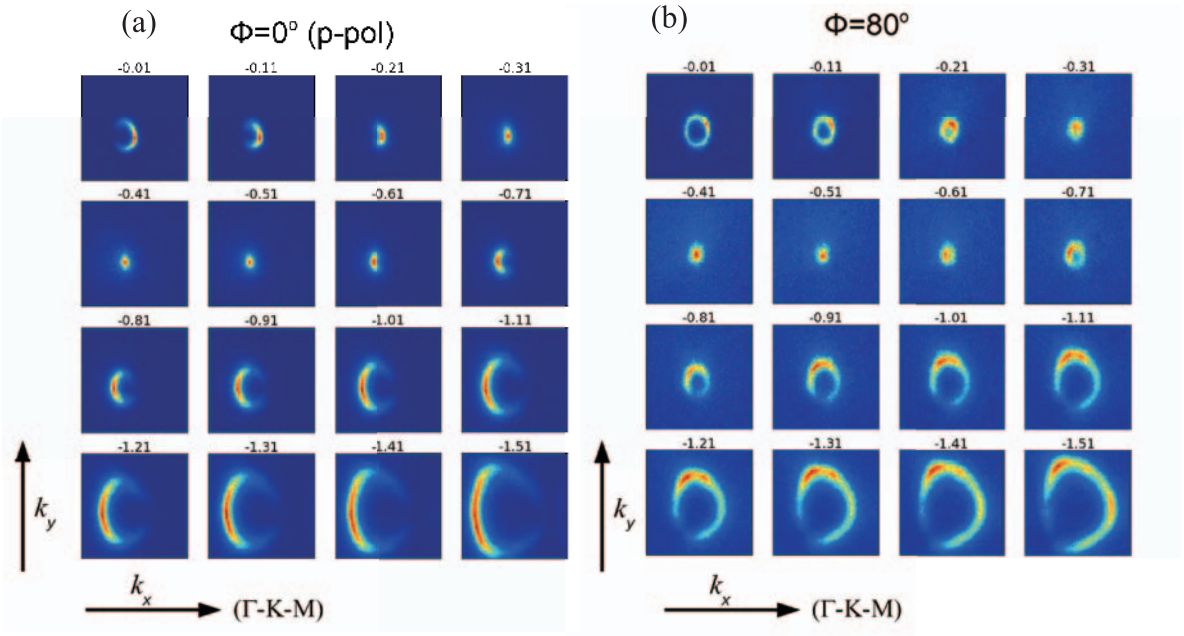

Fig. 2 : ARPES intensity distribution map of the Dirac cone of the single-layer graphene as a function of the binding energy taken at hν=47eV. The polarization angle ϕ=0 (p-pol) (a) and 80° (b).

shown follows. In the case of the p-polarized light [Figs. 2(a)], the intensities can be described by a simple function of the phase θ_q; that is $I(\vartheta_q) = I_N \sin^2(\vartheta_q/2)$, where I_N denotes the intensity normalization factor, for the binding energies below the Dirac point or $I(\vartheta_q) = I_N \cos^2(\vartheta_q/2)$ for those above the Dirac point. When the s-polarization light is used (not shown), the intensity distribution is completely opposite, i.e., $I(\vartheta_q) = I_N \cos^2(\vartheta_q/2)$ bellow the Dirac point and $I(\vartheta_q) = I_N \sin^2(\vartheta_q/2)$ above the Dirac point. These distributions have been observed previously, and well explained with theories [1].

On the other hand, the intensity distribution of the photoelectron is so simple when the polarization angle ϕ=80°. The intensity distribution changes drastically with changing the binding energy. Above the Dirac point, there are no θq where the intensity is extinguished. Below the Dirac point, the photoelectron intensity is extinguished at a certain θq, which is dependent of the binding energy. In fact, the intensity distribution rotates around the K-point with increasing the binding energy, and a clear spiral form emerges in the intensity distribution This kind of structure in the photoelectron intensity distribution has never observed to the best of my knowledge. It should be noted that the intensity distributions cannot produced by simple rotations of the $\cos^2(\vartheta_q/2)$ distribution but a more complicated formula would be necessary.

There are two factors which seem responsible for this unique property in the photoelectron intensity distribution at ϕ=80°. First, since the photoelectron intensity is determined by the matrix element $\langle \varphi_f | H_{opt} | \varphi_i \rangle$, which are different between the s-polarized light and p-polarized light, and ratio of them are dependent on the binding energy of the final state of the photoexcitation [2]. This factor can provide a change in the photoelectron distribution as a function of the binding energy. However, the spiral form cannot be produced by the linear combination of the $\cos^2(\vartheta_q/2)$ and $\sin^2(\vartheta_q/2)$ at all. Thus, another factor should be taken into account. The geometry of the experiments requires the non-normal incidence of the photon beam, and the values of the phase-shift in the electromagnetic wave at the reflection are different between s- and p-polarized lights. The combination of the s- and p-polarized lights will thus yield circularly-polarized light when the phase is shifted to each other. It is known that circularly polarized light produces the photoelectron distribution in the form $\sin^2(\vartheta_q/2+\psi)$ in graphene, where ψ is the rotation angle[1]. These two factors should be considered simultaneously for interpreting the intensity distribution. Quantitative analysis is in progress.

1. M. Mucha-Kruczyński *et al.*, Phys. Rev. B 77, 195403 (2008); Y. Liu *et al.* Phys. Rev. Lett. 107 166803 (2011); I. Gierz *et al.* Phys. Rev. B 83 121408(R) (2011) ; C. Hwang *et al.*, Phys Rev. B 84 125422 (2011); I. Gierz *et al.*, Nano Lett. 12 3900 (2012);
2. Pourya Ayria *et. al.*, . Phys. Rev. B. 92, 195148 (2015).

15-A-18 BL-1

Symmetry-Resolved Surface-Derived Electronic Structure of WSe_2

Iori Tanabe[a], Takashi Komesu[a], Eike F. Schwier[b], Yohei Kojima[b], Mingtian Zheng[b], Hideaki Iwasawa[b], Kenya Shimada[b], Duy Le,[c] Talat Rahman[c] and Peter A. Dowben[a]

[a]*Department of Physics and Astronomy, Nebraska Center for Materials and Nanoscience, Theodore Jorgensen Hall, 855 N 16th, University of Nebraska, 880299, Lincoln, NE 68588-0299, U.S.A.*
[b]*Hiroshima Synchrotron Radiation Center, Hiroshima University, Higashi-Hiroshima 739-0046, Japan*
[c]*Department of Physics, University of Central Florida, 4000 Central Florida Blvd., Orlando, FL 32816 U.S.A.*

Keywords: Angle Resolved High Resolution Photoemission Spectroscopy, Electronic Structure, Symmetry Assignment, Spin-Orbital Coupling.

Monolayer MoS_2 and the related metal dichalcogenides (MX_2, where M = Mo, W and X = S, Se) all share a hexagonal symmetry with graphene, and can exist in the thin film limit of one layer [1]. Of interest to us is the very large spin-orbit coupling (SOC) [1], especially for WSe_2. In this way, WSe_2 combines several of the major advantages of graphene and III-V semiconductors, and unlike MoS_2, WSe_2 is both p-type and has a wider gap of a spin orbit coupling.

The band structure of WSe_2(0001) [2-6] and monolayer WSe_2 [2,3,6-10] has been much studied, although not as heavily investigated as other related metal dichalcogenide such as MoS_2(0001) [2,7-10], and yet the investigation of band symmetry has not been an emphasis in prior experimental work.

In this study, we have done high-resolution angle resolved photoemission spectroscopy (HR-ARPES) measurements at HiSOR BL-1 to identify the surface electronic band symmetry and the wave vector dependent band gap of WSe_2(0001). We measured HR-ARPES with similar setup of experimental geometry of MoS_2 performed in 2014. Multiple WSe_2(0001) samples were cleaved in-situ, and the energy was referred to the Fermi level of Co film electrically connected to the sample.

Figure 1 shows HR-ARPES results of a) s-polarization, and b) p-polarization geometries. The incident photon energy was set at 34 eV, and the sample temperature was at room temperature. One can see clear difference between these two results. This is very clear evidence of the retention of wave vector dependent state symmetry in individual bands, and similar to those results acquired with MoS_2. By acquiring such comparable data sets with p-, and s-polarization geometries, each dispersing band can be assigned to a particular symmetry by comparison with the results of DFT calculations, indicated in dashed lines in Figure 1. The dispersions of several bands are easily discerned and we find that the symmetry is in fact wave vector dependent due to overlapping wave vector dependent spectral weight contributions.

The comparison of theory and experiment provides strong indications that the bands at the top of the valence band are dominated by W 4d states. These valence bands can be perturbed by adsorbates. Indeed, as with our previous studies of MoS_2, we found that, the valence band structure of WSe_2(0001) was shifted as much as 0.1 eV away from the Fermi level, after Na adsorption, which clearly indicates the Na atoms donate electrons to WSe_2. Surprisingly, Na adsorption does not significantly perturb the WSe_2 band dispersion, as also seen on the case of MoS_2, and the shifts are rigid-band like. Addition to such Na adsorption, in this study, we performed Co adsorption studies, and Co adsorption shows a rigid shift of the transition metal dichalcogenide bands to smaller binding

energies (the opposite direction seen with Na adsorption). This is the strong indication of an extrinsic n-type doping with Co adsorption onto the WSe_2 and MoS_2 systems.

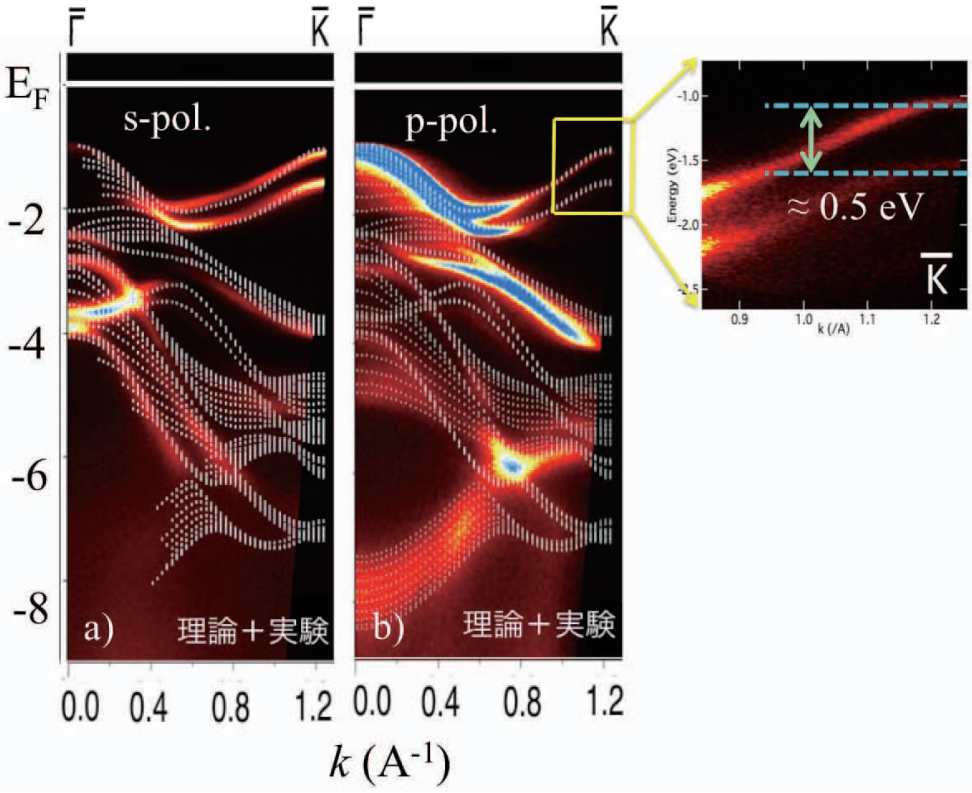

Fig. 1. Showing the angle resolved photoemission spectroscopy results, taken at HiSOR BL-1, with 34 eV photon energy with a) s-polarization and b) p-polarization photoemission geometries. Comparison is made with DFT theoretical calculations, indicated by dashed lines. The right side inset is showing a spin orbital splitting, about 0.5 eV at $\overline{\mathrm{K}}$ point.

REFERENCES

[1] Mak K F, Lee C, Hone J, Shan J, Heinz T F 2010 *Phys. Rev. Lett.* **105** 136805.
[2] Yun W S, Han S, Hong S C, Kim I G, Lee J 2012 *Phys. Rev. B* **85** 033305.
[3] Yeh P-C, Jin W, Zaki N, Zhang D, Liou J T, Sadowski J T, Al-Mahboob A, Dadap J I, Herman I P, Sutter P, Osgood R M 2015 *Phys. Rev. B* **91** 041407(R).
[4] Yu S W, Lischke T, David R, Muller N, Heinzmann U, Pettenkofer C, Klein A, Perlov A Y, Krasovskii E E, Schattke W, Braun J 1999 *Journal of Electron Spectroscopy and Related Phenomena* **101** 449-54.
[5] Finteis T, Hengsberger M, Straub T, Fauth K, Claessen R, Auer P, Steiner P, Hüfner S, Blaha P, Vögt M, Lux-Steiner M, Bucher E 1997 *Phys. Rev. B* **55** 10400–11.
[6] Yuan H, Bahramy M S, Morimoto K, Wu S, Nomura K, Yang B-J, Shimotani H, Suzuki R, Toh M, Kloc C, Xu X, Arita R, Nagaosa N, Iwasa Y 2013 *Nat. Phys.* **9** 563–9.
[7] Kormányos A, Burkard G, Gmitra M, Fabian J, Zólyomi V, Drummond N D and Fal'ko V 2015 *2D Mater.* **2** 022001.
[8] Klots A R, Newaz A K M, Wang B, Prasai D, Krzyzanowska H, Lin J, Caudel D, Ghimire N J, Yan J, Ivanov B L, Velizhanin K A, Burger A, Mandrus D G, Tolk N H, Pantelides S T, Bolotin K I 2014 *Sci. Repts.* **4**, 6608.
[9] Kozawa D, Kumar R, Carvalho A, Amara K K, Zhao W, Wang S, Toh M, Ribeiro R M, Castro Neto A H, Matsuda K, Eda G 2014 *Nat. Commun.* **5**, 4543.
[10] Ramasubramaniam A 2012 *Physical Review B* **86** 115409.

Large area, nearly free-standing monolayer graphene on Pt

Wei Yao[a], Eryin Wang[a], Alexei V. Fedorov[c], Eike F. Schwier[d], Hideaki Iwasawa[d], Kenya Shimada[d], and Shuyun Zhou[a,b,*]

[a] *State Key Laboratory of Low Dimensional Quantum Physics and Department of Physics, Tsinghua University, Beijing 100084, China*

[b] *Collaborative Innovation Center of Quantum Matter, Beijing, P.R. China*

[c] *Advanced Light Source, Lawrence Berkeley National Laboratory, Berkeley, CA 94720, USA*

[d] *Hiroshima Synchrotron Radiation Center, Hiroshima University, Higashi-Hiroshima 739-0046, Japan*

Keywords: graphene, Pt(111), monolayer, free-standing

Finding a reliable method for producing large area, high quality graphene is fundamental to realize its potential applications, and efforts to improve the graphene quality still continue. Epitaxial growth of graphene on transition metals has been considered as a promising route. However, the interaction between graphene and metal substrates often results in strong modifications of the graphene properties, and is a major problem that needs to be overcome [1-3]. Here we report a new synthesis method of graphene on Pt(111) substrate. Using various techniques including low energy electron diffraction (LEED), X-ray photoemission spectroscopy (XPS), and ARPES, we show that the graphene grown by the new method is monolayer thick, high quality, charge neutral and behaves like free standing graphene. Such graphene sample provides an important platform to investigate the intrinsic properties of graphene, and may be useful for applications when combined with nondestructive sample transfer techniques.

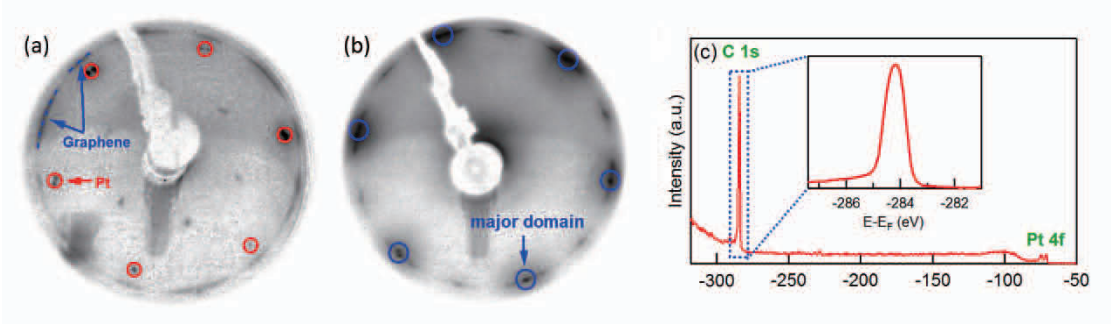

FIGURE 1: (a), (b) LEED patterns at different temperatures ((a) below 1000 ^{0}C and (b) above 1000 ^{0}C). (c) XPS spectrum of Pt(111) after annealing above 1000 ^{0}C measured at photon energy of 360 eV. Carbon 1s peak around binding energy of 284 eV and platinum 4f peaks around 73 eV are marked. The inset is the zoom-in of the Carbon 1s peak. From Ref.[4]

Figure 1 shows the characterization of the graphene sample using LEED and XPS. At initial stage, spots from substrate coexist with the ring pattern from graphene, showing multi-orientation of graphene and hence the weak graphene-substrate inter-action. At high temperature, the pattern from substrate disappears and one major orientation emerges from the ring pattern of graphene. This means the graphene develops into a dominated ordered structure. The characterized carbon 1s peak in X-ray

photoemission spectrum confirm that we have succeeded growing graphene on Pt(111) by the new method [4].

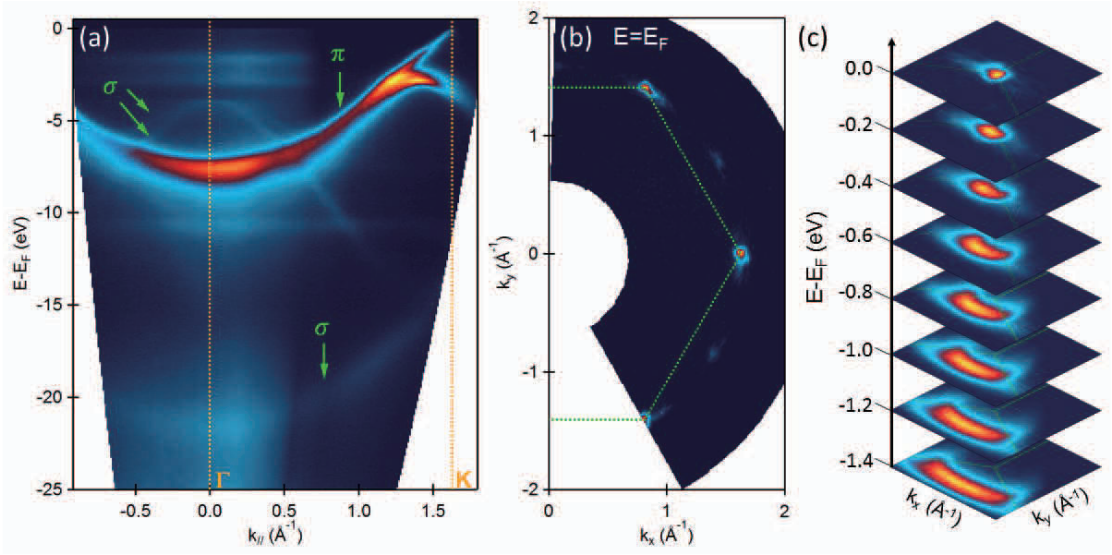

FIGURE 2: (a) Band structure of the graphene on Pt(111) along Γ- K direction measured by ARPES. The clear π band and σ band are indicated by the green arrow. The other π band comes from another domain. (b) Measured point-like Fermi surface map of the graphene. The two set of Dirac points come from two domains respectively. (c) Clear linear dispersion (Dirac cone) goes across Fermi energy at K point.

Figure 2 shows the electronic structure from ARPES measurements. Figure 2(a) shows the valence band measured along Γ-K direction. The characteristic π bands and σ bands of graphene are observed, confirming that its electronic structure is identical to graphene. Different from graphene grown on other metal substrates [3, 4], the graphene sample on Pt(111) substrate shows negligible signal from the substrate bands and there is no discernible modification of the band structure, reflecting that the graphene behaves like free-standing graphene. Figure 2(b) shows the measured Fermi surface of graphene. The observation of a stronger set of Dirac cones and a weaker one is consistent with LEED pattern. Figure 2(c) shows the conical dispersion at the K point. The point-like Fermi surface shows that the graphene is almost charge neutral and there is negligible charge transfer from the substrate. No splitting of the cones is observed, suggesting that the graphene sample is monolayer thick. We find that the graphene sample is very stable, and survives in the air. After reloading to the vacuum chamber and annealing at 400 ^{0}C, sharp graphene dispersions can be observed again.

To summarize, we discover a new growth method of growing graphene on Pt(111). The properties of this graphene resemble the ideal free-standing monolayer graphene. It has weak interaction with substrate, and therefore less charge transfer, leading to a nearly neutral doping level with very week electron-phonon interaction. Such a graphene system provides a new platform investigate the properties of the ideal graphene. This work has been published in Phys. Rev. B [4].

References:

1. Soren Ulstrup *et al.*, Phys. Rev. B., **88**, 125425 (2013).

2. I. Pletikosic *et al.*, Phys. Rev. Lett., **102**, 056808 (2009).

3. E. Starodub *et al.*, Phys. Rev. B., **83**, 125428 (2011).

4. W. Yao *et al.*, Phys. Rev. B. **92**, 115421 (2015)

Spin- and angle-resolved photoemission study of oxygen adsorbed Fe/MgO(100)

Mingtian Zheng[a], Eike F. Schwier[b], Koji Miyamoto[b], Taichi Okuda[b], Kenya Shimada[b], Hideaki Iwasawa[b], Taiki Horike[a], Yorito Nagata[a], Yohei Kojima[a], Hirofumi Namatame[b], and Masaki Taniguchi[a,b]

[a]*Graduate School of Science, Hiroshima University, Higashi-Hiroshima 739-8526, Japan*
[b]*Hiroshima Synchrotron Radiation Center, Hiroshima University, Higashi-Hiroshima 739-0046, Japan*

Keywords: Fe(100)-*p*(1×1)-O surface, Fermi surface, surface states

The oxygen adsorbed iron surface, Fe(100)-*p*(1×1)-O (O-Fe), is stable and used as a target material for the high-efficiency spin detector [1]. While the scattering properties of the surface are widely examined, the Fermi surfaces and electronic band dispersions have not been revealed in detail so far. We assume that the physical properties of O-Fe is closely related to the adsorption of oxygen at surface. For this purpose, the study the adsorption effects on Fe(100) are important. The band dispersions on pure Fe(100) have been examined by spin-resolved or spin-integrated angle-resolved photoemission spectroscopy (ARPES) [2,3]. Recently, we have successfully performed high-resolution angle-resolved photoemission spectroscopy experiments of pure Fe and O-Fe films grown on MgO at HiSOR BL-1[5]. In our previous study, we have observed the detailed Fermi surfaces and band dispersions in thorough surface Brillouin zone with high energy and momentum resolutions, the effects of oxygen adsorption on band dispersions close to Fermi edge (E_F) had been studied.

However, the details of surface states still remain to be investigated in order to understand the spin-transition properties, the evolution of Fe surface state during oxygen adsorption will also help to explain the oxygen adsorption effects on Fe. Moreover, until recently, there has been no study on the Fermi surface nor high resolution studies of the band dispersions close to E_F on the oxygen adsorbed Fe so far.

In this study, we have successfully performed high-resolution ARPES experiments of both pure Fe and oxygen adsorbed O-Fe thin films grown on MgO, studied the effects of oxygen adsorption and the surface state of pure Fe. The experiments were done at the HiSOR BL-1. Single crystalline Fe(100) films on MgO(100) substrates were prepared under ultrahigh vacuum conditions.

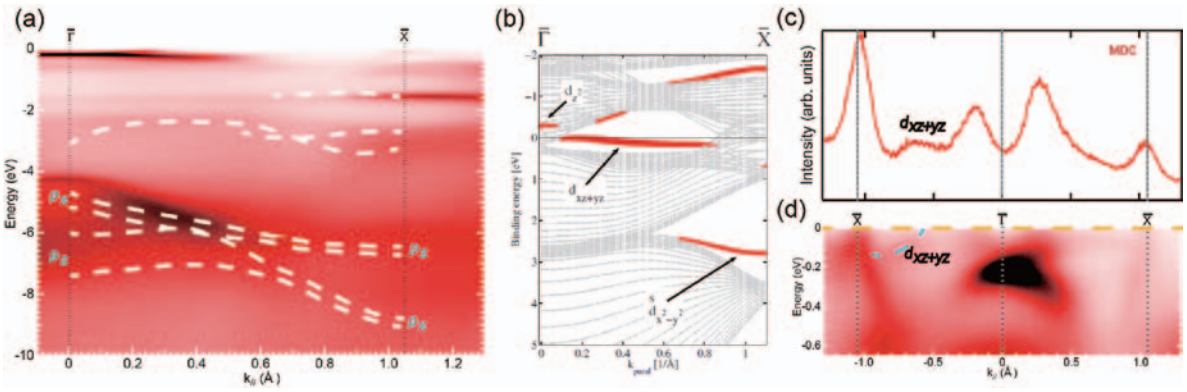

FIGURE 1. (a) Valance band dispersions of oxygen adsorbed Fe(100)-*p*(1×1)-O surface taken with *p*-polarization geometry (with dashed lines: spin-ARPES results [4]). (b) Calculated surface states on pure Fe [3]. (c) MDC at E_F and (d) band dispersions close to E_F along the $\bar{\Gamma}$ $\bar{X}$ high-symmetry line of oxygen adsorbed Fe(100)-*p*(1×1)-O surface taken with *p*-polarization geometry.

Fig. 1(a) shows the ARPES image of Fe(100)-p(1×1)-O valance band along the $\bar{\Gamma}$ $\bar{X}$ high-symmetry line, compared with previous spin-ARPES results. It is observed the *p-d* hybridization states exist between -1 to -4

eV and between -4 to -9 eV, [4] while oxygen *2p* bands splitted between -4 to -9 eV. We can also observe the surface resonance states at binding energy between -2.5 eV to -3.5 eV at the $\bar{X}$-point.

Fig. 1(b) shows a theoretical result [3]: a Fe d_{xz+yz} surface state cross E_F exists along $\bar{\Gamma}$ $\bar{X}$ high symmetry line. Figs. 1(c) and 1(d) show the experimental observation of the state, the peak at MDC at E_F and band dispersions from the ARPES image clearly proved the existence of d_{xz+yz} surface state. Moreover, comparison between band dispersions and Fermi surface mapping of pure Fe(100) and O-Fe(100) shows clear changes with respect to the Fe d_{xz+yz} surface state along $\bar{\Gamma}$ $\bar{X}$ high symmetry line.

Comparison with preliminary slab calculations [3,5] hints to minority as well as majority spin polarizations of the states around the $\bar{\Gamma}$-point. To reveal the spin polarization of the fine structure close to E_F, we performed spin-resolved ARPES at HiSOR BL-9B, using the He lamp (hν=21.2 eV). The *ex-situ* stored samples were reprepared by flashing the thin film in vacuum. Spin-resolved and spin-integrated ARPES were performed at low temperature. The linewidth of band dispersions from *in-situ* prepared samples and reprepared *ex-situ* stored samples were almost comparable.

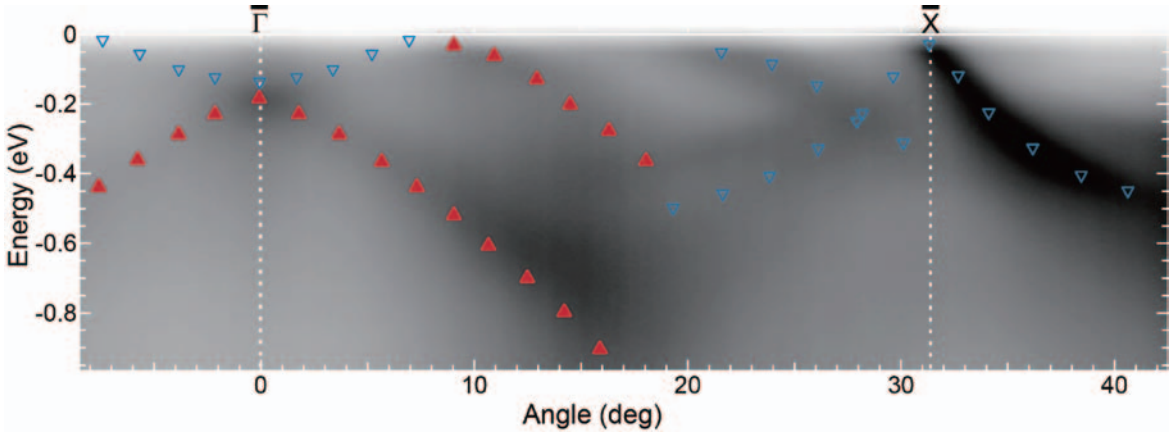

FIGURE 2. Spin-resolved ARPES results of band dispersions close to E_F along the $\bar{\Gamma}$ $\bar{X}$ high-symmetry line of oxygen adsorbed Fe(100)-*p*(1×1)-O surface taken with He-I. The red triangle marks shows the spin up states while the blue triangle marks shows the spin down states.

Fig. 2 shows the APRES image of band dispersions close to E_F along the $\bar{\Gamma}$ $\bar{X}$ high-symmetry line with spin-resolved ARPES results marked on it. It's clear the states around $\bar{\Gamma}$-point are spin polarized, the electron like band cross E_F is spin down state, while the state under the first one is spin up state. The results also show the hole-like state around the $\bar{X}$-point is spin down state. These results are corresponding to the calculation prediction, gives us new detailed experimental view on the fine electron structure of Fe close E_F.

REFERENCES

1. T. Okuda et al., Rev. Sci. Instrum. 82, 103302 (2011).
2. A. M. Turner, Yu Jeng Chang, and J. L. Erskine, Phys. Rev. Lett. 48, 348 (1982).
3. L. Plucinski et al., Phys. Rev. B 80, 184430 (2009).
4. N. B. Brookes et al. Phys. Rev. B 41, 9659 (1990)
5. E. F. Schwier, unpublished work.

15-A-65 BL-1

ARPES studies on the electronic structure of a new diluted ferromagnetic semiconductor with Curie temperature up to 230K

Yong Hu[a] , Yu Xu[a], Shaolong He[a], Mingtian Zheng [b], E. F. Schwier [b], H. Iwasawa [b], K. Shimada [b], H. Namatame [b] and Xingjiang Zhou[a]

[a]*National Lab for Superconductivity, Beijing National Laboratory for Condensed Matter Physics, Institute of Physics, Chinese Academy of Sciences, Beijing100190, China*
[b] *Hiroshima Synchrotron Radiation Center Hiroshima University 2-313 Kagamiyama, Higashi-Hiroshima City, 739-0046 JAPAN*

Keywords: Dilute ferromagnetic semiconductor, ARPES,

Diluted magnetic semiconductors (DMSs) have attracted considerable attention due to their potential applications for future spintronic devices [1-5]. However, despite several decades of intensive research efforts, challenges remain and materials complexity still hinders theoretical understanding. The origin of magnetic ordering and paths to higher curie temperature Tc remain strongly debates [2, 6,7].

The recent discovery of DMS material, $Ba_{1-x}K_x(Zn_{1-y}Mn_y)_2As_2$ [8] (Mn-$BaZn_2As_2$), is isostructural to the "122"-family iron-based high temperature superconductors [9] and has a curie temperature Tc as high as 230 K [10]. This material has the advantage that the Ba layer, where hole carriers are generated, and the ZnAs layer, where magnetic elements are introduced, are spatially separated. This allows one independently control the concentration of charge carriers and magnetic elements.

The dual role of Mn in DMS compounds like $Ga_{1-x}Mn_xAs$ complicates theoretical understanding, including whether double exchange [11] is a relevant mechanism in these systems. The argument against double exchange is that it requires either different charge states [12] on Mn and/or the presence of an impurity band [13]. This controversy over the exchange mechanism might be solved in the new DMS because this recently discovered class of DMS systems allows one to treat spin and charge doping independently.

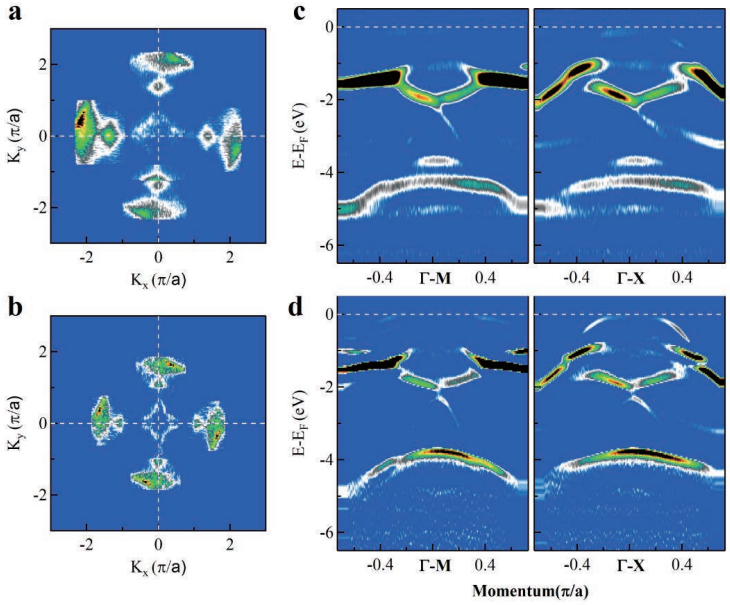

FIGURE 1. Fermi surface and band structure of (Ba, K)(Zn, Mn)As and (Ba, K)ZnAs taken with hv=34eV. (a), (b) Integrated spectral intensity as a function of momentum for (Ba, K)(Zn, Mn)As and (Ba, K)ZnAs, respectively. The images are obtained by integrating the spectral weight over a small energy window [-0.03 eV, -0.01 eV]. (c), (d) Band structure for the momentum cuts across Γ-M (c), Γ-X (d). The images are obtained by the second derivative of the original data with respect to the energy.

Figure 1 shows ARPES spectra taken with hv=34eV. Figure 1 (a), (b) show the "Fermi surface" of $Ba_{1-x}K_x(Zn_{1-y}Mn_y)_2As_2$ and $Ba_{1-x}K_xZnAs$, respectively, which are obtained by integrating over a small energy window ranging from -0.03eV and -0.01eV. The band dispersions taken at temperature of 30K along the high symmetry directions labeled as Γ-M and Γ-X in figure 1 (c) and (d).

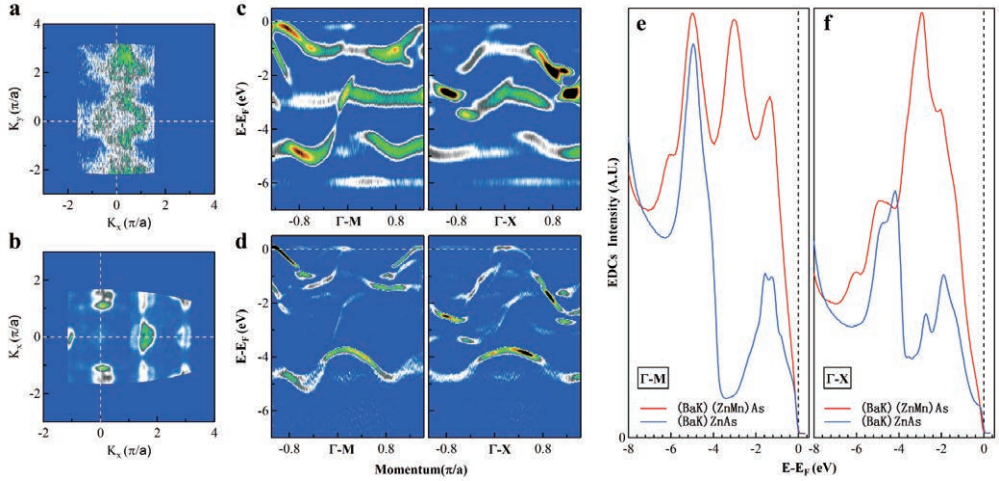

FIGURE 2. Fermi surface and band structure of $Ba_{1-x}K_x(Zn_{1-y}Mn_y)_2As_2$ and $Ba_{1-x}K_xZnAs$ taken with hv=95eV. (a), (b) Integrated spectral intensity as a function of momentum for $Ba_{1-x}K_x(Zn_{1-y}Mn_y)_2As_2$ and $Ba_{1-x}K_xZnAs$, respectively. The images are obtained by integrating the spectral weight over a small energy window [-0.03 eV, -0.01 eV]. (c), (d) Band structure for the momentum cuts across Γ-M (c), Γ-X (d). The images are obtained by the second derivative of the original data with respect to the energy. (e), (f) Integrated energy distribution curves (EDCs) for the momentum cuts across Γ-M (c) and Γ-X (d), respectively.

In order to clarify the Mn 3d-derived states, we try to change photon energy. Figure 2 shows ARPES results taken with, hv=95eV, keeping the sample temperature at 30K during the measurements. Constant energy mapping at E_F is shown in Fig. 1 (a) and (b), which are obtained by integrating over a small energy window ranging from -0.03eV and -0.01eV for $Ba_{1-x}K_x(Zn_{1-y}Mn_y)_2As_2$ and $Ba_{1-x}K_xZnAs$, respectively. Comparing with figure (c) and (d), we observe an nondispersive intensity due to Mn 3d states around 6eV blew the Fermi level in $Ba_{1-x}K_x(Zn_{1-y}Mn_y)_2As_2$, which also can be found in integrated EDCs shown in figure 2 (e).

REFERENCES

1. Ohno, H. Making nonmagnetic semiconductors ferromagnetic. *Science* 281, 951-956 (1998).
2. Dietl, T. A ten-year perspective on dilute magnetic semiconductors and oxides. *Nat. Mater.* 9, 965-974 (2010).
3. Zutic, I., Fabian, J & Das Sarma, S. Spintronics: fundamentals and applications. *Rev. Mod. Phys.* 76, 323-410 (2004).
4. Ohno, H. et al. (Ga, Mn)As: A new diluted magnetic semiconductor based on GaAs. *Appl. Phys. Lett* 69, 363-365 (1996).
5. Dietl, T. et al. Zener model description of ferromagnetism in zinc-blende magnetic semiconductors. *Science* 587, 1019-1022 (2000).
6. M. Tanaka, S. Ohya, and P. N. Hai, Appl. Phys. Rev. 1, 011102 (2014).
7. M. Dobrowolska, K. Tivakornsasithorn, X. Liu, J. Furdyna, M. Berciu, K. M. Yu, and W. Waluliewicz, *Nat. Mater.* 11, 444 (2012).
8. K. Zhao, Z. Deng, X. C. Wang, W. Han, J. L. Zhu, X. Li, Q. Q. Liu, R. C. Yu, T. Goko, B. Frandsen, L. Liu, F. Ning, Y. J. Uemura, H. Dabkowska, G. M. Luke, H. Luetkens, E. Morenzoni, S. R. Dunsiger, A. Senyshyn, P. Bni, and C. Q. Jin, *Nat. Commun.* 4, 1442 (2013).
9. J. Paglione and R. L. Greene, Nat. Phys. 6, 645 (2010).
10. K. Zhao, B. Chen, G. Zhao, Z. Yuan, Q. Liu, Z. Deng, J. Zhu, and C. Jin, *Chin. Sci. Bull.* 59, 2524 (2014).
11. D. Khomskii, Basic Aspects of the Quantum Theory of Solids (Cambridge University Press, Cambridge, U.K., 2010).
12. T. Dietl and H. Ohno, *Rev. Mod. Phys.* 86, 187 (2014).
13. T. Jungwirth, J. Sinova, J. Ma˘sek, J. Kucera, and A. H. MacDonald, *Rev. Mod. Phys.* 78, 809 (2006).

15-B-20 BL-1

Electron Doping to Rutile TiO_2 Surface by Na Deposition

R.-Y. Liu[a], K. Ozawa[b], E. F. Schwier[c], M. Zheng[c], H. Iwasawa[c], K. Shimada[c], H. Namatame[c], M. Taniguchi[c], I. Matsuda[a], Y. Aiura[d]

[a]*Institute for Solid State Physics, The University of Tokyo, Kashiwa, Chiba 27-8581, Japan*
[b]*Department of Chemistry, Tokyo Institute of Technology, Meguro, Tokyo 152-8551, Japan*
[c]*Hiroshima Synchrotron Radiation Center, Hiroshima University, Higashi-Hiroshima, Hiroshima 739-0046, Japan*
[d]*National Institute of Advanced Industrial Science and Technology, Tsukuba, Ibaraki 305-8568, Japan*

Keywords: rutile TiO_2, in-gap state, band bending, photoelectron spectroscopy, *in situ* deposition

INTRODUCTION

Manipulation of the electronic structures by carrier doping is a fundamental technique to tune the opto- and magnetoelectronic properties of semiconductors. Since the discovery of the two-dimensional electron gas (2DEG) at the $LaAlO_3/SrTiO_3$ interface [1], metallization via the emergence of 2DEG at oxide-oxide interfaces and oxide surfaces has attracted considerable attention in order to elucidate the formation mechanism as well as the nature of the 2DEGs for future oxide-based devices. 2DEG systems with a metallic nature at oxide surfaces are realized when the electrons are doped to the surfaces of n-type oxides such as $SrTiO_3$ [2], ZnO [3], TiO_2 [4], etc. The commonly accepted mechanism of the 2DEG formation is that, as the electrons are doped to the oxide surface by the formation of O vacancies on the surface or deposition of electron dopants on the surfaces, downward bending of valence and conduction bands is induced at the surface to form an accumulation layer. The doped electrons are trapped within this layer and show a free-electron-like behavior along the surface parallel direction. As the magnitude of downward band bending is so large that the conduction band minimum (CBM) moves below the Fermi level, the 2DEG with a metallic nature is realized.

It is known that TiO_2 exhibits different physicochemical properties depending on its crystal structure [5]. For example, the band gap of anatase TiO_2 is slightly larger than that of rutile TiO_2. Electron mobility is higher in anatase TiO_2 than in rutile TiO_2. These differences may explain the higher photocatalytic activity of anatase TiO_2 than rutile TiO_2. Response to the electron doping is also structure dependent. Electron doping and the resultant metallic 2DEG have been reported only on the surfaces of anatase TiO_2 [4], but not on the rutile surfaces.

The present study aims to answer the question: "Is the 2DEG really not formed on the rutile TiO_2 surfaces?" Change in the electronic structure of the rutile TiO_2 surface has been investigated by photoelectron spectroscopy (PES) while the electrons are doped to the surface by Na deposition. Special attention has been payed to the position of the valence band maximum (VBM), the density of states (DOS) around the Fermi level as well as the Ti 3d state formed within the band gap. Although electron doping results in downward bending of the TiO_2 band to form an accumulation layer at the surface, the doped electrons are localized at the Ti sites to suppress the free-electron-like behavior in the accumulation layer.

EXPERIMENTAL

The experiment was carried out at BL-1. Single crystal rutile TiO_2 with (011) orientation (MTI co.) was used. The surface was cleaned by cycles of Ar^+ sputtering (an ion beam energy of 2 kV) and annealing in O_2 atmosphere (2×10^{-4} Pa) at 900 K. The cleanliness was checked by Auger electron spectroscopy measurements. The clean TiO_2(011) surface exhibited sharp (2×1) low energy electron diffraction spots. Na was deposited on the surface using a commercial Na dispenser (SAES Getters). The sample temperature was kept at 150 K during Na deposition and the PES measurements.

RESULT AND DISCUSSION

The PES spectra of TiO_2 in the valence band region is characterized by O 2p-dominated O 2p-Ti 3d hybridized bands between 3 and 9 eV and a weak DOS within the band-gap region (called "in-gap state" hereafter). Fig. 1 shows an intensity map of the valence band of the TiO_2(011)-2×1 surface. The VBM position,

determined by extrapolating the leading edge of the O 2p-Ti 3d bands to the base line, is found at 3.74 eV, and the in-gap state lies at 0.94 eV without an apparent energy dispersion. The in-gap state is associated with the Ti 3d state of Ti^{3+}, which is formed upon the formation of the oxygen vacancies or electron doping at the surface and the resultant reduction of Ti^{4+}. Thus, the intensity of the in-gap state is proportional to the density of Ti^{3+}.

When Na is deposited on the surface, the in-gap state grows almost linearly as shown in Fig. 2. At the same time, the VBM position moves from 3.74 eV (on the clean surface) to 3.86 eV. Considering the band gap of rutile TiO_2 (3.0 eV), the CBM should be at 0.86 eV below the Fermi level. These spectral changes indicate that Na donates its 3s valence electron to the TiO_2 surface and induces downward band bending to form an accumulation layer at the surface. The amount of donated charge is evaluated from the magnitude of Na-induced band bending (0.12 eV) to be 3×10^{15} cm^{-2}.

When we closely examine the spectral lineshape at the Fermi level, it appears that the DOS at the Fermi level remains low even after the sufficient amount of the electrons is doped. Thus, the 2DEG with a metallic property is not developed on the TiO_2(011)-2×1 surface. So, where do the doped electrons go? Because the intensity of the in-gap state is proportional to the density of Ti^{3+}, and because the in-gap state grows with Na deposition (Fig. 2), the doped electrons should be localized at the Ti 3d state of Ti^{4+} to form Ti^{3+}. The highly localized picture of the excess electrons on the TiO_2(011)-2×1 surface is in good agreement with the fact that the doped electrons in rutile TiO_2 form small polarons [6, 7].

Essentially the same results is obtained when the electrons are doped to TiO_2(011)-2×1 by H adsorption as well as by O vacancy formation [8]. Irrespective of the doping techniques, the excess electrons reside at the Ti sites without forming the 2DEG on the surface.

The behavior of the excess electrons on the rutile surface is in sharp contrast to that on the anatase surface. Rödel et al. have found from their PES study [4] that free-electron-like metallic bands are developed on anatase TiO_2(101) and (001) when electrons with densities of the order of 10^{13}—10^{14} cm^{-2} are doped to the surfaces. Unlike the electrons in rutile TiO_2, the excess electrons in anatase TiO_2 prefer to behave as free carriers rather than to form the polarons because the energy gain by the polaron formation is less in anatase TiO_2 than in rutile TiO_2 [7].

SUMMARY

The PES is utilized to examine the behavior of doped electrons on rutile TiO_2(011)-2×1. Electron doping induces downward band bending and results in an accumulation layer at the surface. The electrons are, however, highly localized at the Ti sites within the layer. This hampers the formation the 2DEG at the surface even at the relatively high doping level.

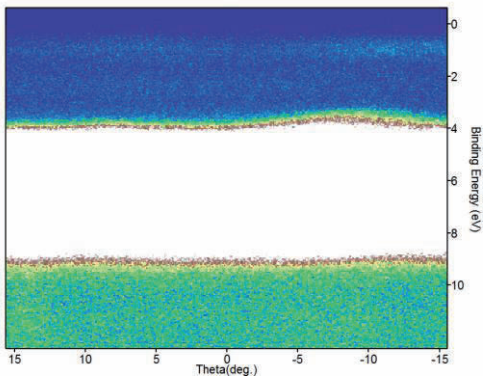

FIGURE 1. Intensity map of the valence band region of the clean TiO_2(011)-2×1 surface. The photon energy used was 73 eV.

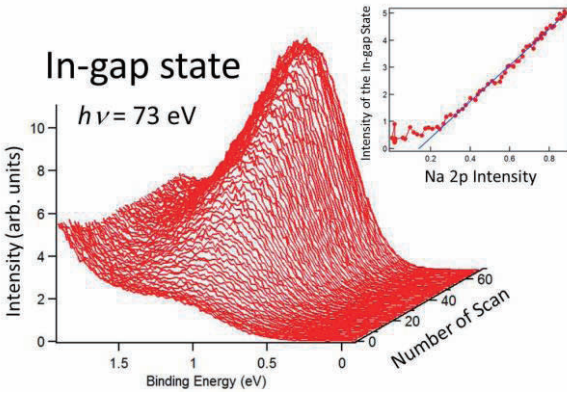

FIGURE 2. Evolution of the in-gap state upon Na deposition. The inset shows the intensity variation of the in-gap state as a function of the Na 2p peak intensity.

REFERENCES

1. A. Ohtomo and H. Y. Hwang, *Nature* **427**, 423-426 (2004).
2. A. F. Santander-Syro et al., *Nature* **469**, 189-193 (2011): W. Meevasana et al., *Nature Mater.* **10**, 114-118 (2011).
3. K. Ozawa and K. Mase, Phys. Rev. B 81, 205322 (2010): L. F. J. Piper et al., *Phys. Rev. B* **81**, 233305 (2010).
4. S. Moser et al., *Phys. Rev. Lett.* **110**, 196403 (2013): T. C. Rödel et al., *Phys. Rev. B* **92**, 041106(R) (2015).
5. U. Diebold, *Surf. Sci. Rep.* **48**, 53-229 (2003).
6. H. Tang et al., *J. Appl. Phys.* **75**, 2042-2047 (1994): E. Hendry et al., *Phys. Rev. B* **69**, 081101(R) (2004).
7. M. Setvin et al., *Phys. Rev. Lett.* **113**, 086402 (2014).
8. R.-Y. Liu et al., to be submitted.

14-A-27 BL-1 and 15-B-15 BL-7

Dirac-cone surface state influenced by vicinal surface of W(110)

K. Miyamoto[a, b], C. Lamgenkämper[b], E. F. Schwiwer[a], H. Sato[a],H. Iwasawa[a], K. Shimada[a] and M. Donath[b]

[a] *Hiroshima Synchrotron Radiation Center, Hiroshima University, 2-313 Kagamiyama, Higashi-Hiroshima 739-0046, Japan*

[b] *Physikalisches Institut, Westfälische Wilhelms-Universität Münster, Wilhelm-Klemm-Strasse 10, 48149 Münster, Germany*

Keywords: Dirac-cone surface state, spin-orbit interaction

Non-magnetic materials possess spin-split band influenced by spin-orbit interaction with combination broken space inversion symmetry, which is called as Rashba effect or Dresselhaus effect etc... . Au(111) is well famous as ordinal Rashba system[1]. Even in vicinal surface of Au(111), Rashba spin-split state is remained but modified because of influence of periodic step potential[2-4]. As the consequence, Shochley-type surface state shows spin polarized quantum well state.

Very recently, we have discovered that the surface of W(110) shows a spin-polarized Dirac-cone state within a spin-orbit-induced gap[5], which is reminiscent of a topological surface state[6]. Here, in contrast to so-far studied topological insulators, the surface structure has C_{2v} symmetry. The C_{2v} symmetry strongly influences the dispersion of the Dirac-cone surface state, resulting in a flattened Dirac-cone[7]. This discovery lead another question: this peculiar spin polarized state accepts influenced by periodic step potential of surface or not. In this work, we have observed the electronic structure corresponding to Dirac-like surface state in a vicinal surface W(771).

Clean surfaces of W(771) are obtained by cycle of heating in oxygen atmosphere ($< 2\text{x}10^{-8}$ Pa) at 1500K and a subsequent flashing at 2200 K. The miscut angle of W(771) corresponds to 5.77º. These are evaluated by Aurge electron spectroscopy and low-energy-electron spectroscopy (LEED). It has been confirmed that the observed LEED pattern shows several supper spots around the very shaper (1x1) spot is caused by step edge, as reported by previous work of different vicinal surface W(331) [8]. Angle-resolved photoemission spectroscopy experiments were performed using linear polarized light at beamlines (BL-1 and BL-7) of Hiroshima Syncjrotron Radiation Center. The overall experimental energy and angular resolutions were set to 15 meV and 0.3º, respectively.

Figure 1 shows the electronic structure excited by photon energy (hν) of 43 eV on W(771), along $\overline{\mathbf{\Gamma H}}$. Although, on W(110), Dirac-cone surface state is located just at emission angle (θ) of 0º ($\overline{\mathbf{\Gamma}}$) at 1.25 eV [5, 7], the observed Dirac-cone state does at emission angle of 5.8º. Miscut angle of 5.77º between W(771) and W(110) creates these different positions. The observed bands in W(771) is almost same as those of W(110). This result implies, although W(771) exist step barriers with a periodic of 7 atoms, the Dirac-cone surface state is not influenced by the step barriers. This results is much different from so-far reported vicinal surface of Au(111). For example, the vicinal surface Au(788) shows the Rashba spin-split quantum well states influenced by its periodic step potential. Generally to create such a quantum well state, it is necessary that the conduction electrons confined by the well-typed potential cause backscattering. However, in Dirac-cone surface state, such backscattering is much suppressed as reported by previous work. Therefore, the Dirac-cone surface state

avoids to be modified by periodic potential of vicinal surface. These results becomes a strong evidence of suppression of electron backscattering in W(110) as expected by Ref. [6].

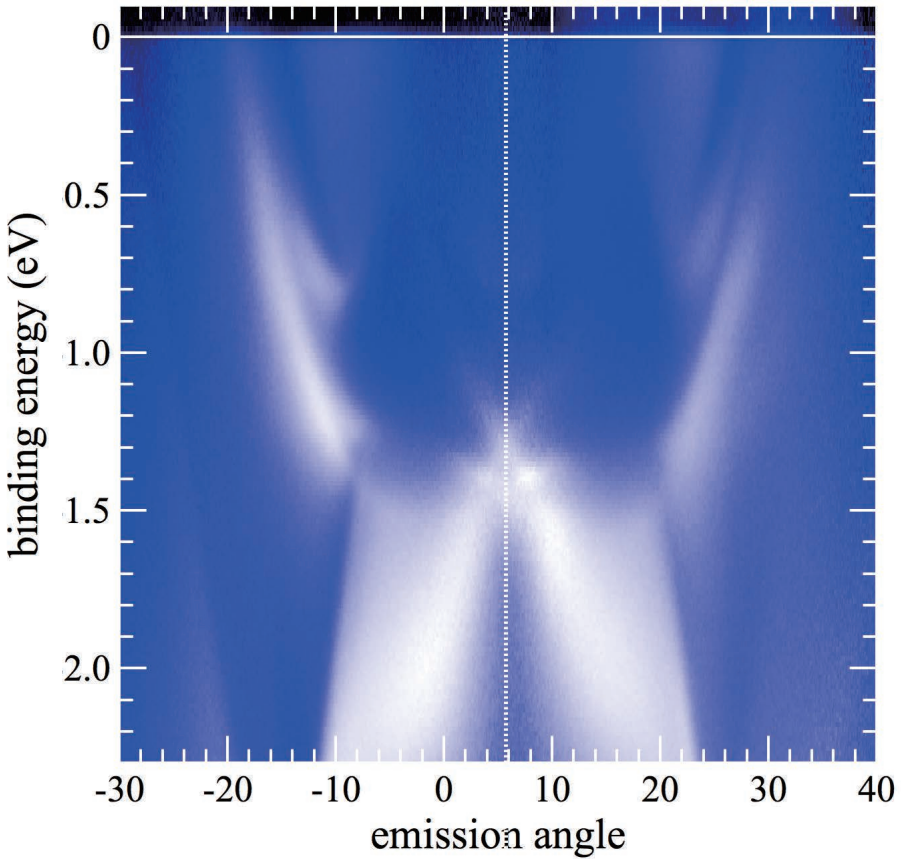

Figure 1 ARPES result for W(771) along $\overline{\Gamma H}$ excited by p-polarized light of hν = 43 eV.

REFERENCES

1. S. LaShell et al., Phys. Rev. Lett. **77**, 3419 (1996).
2. J. E. Ortega, Phys. Rev. B **65**, 165413 (2002).
3. A. Mugarza et al., Phys. Rev. B **66**, 245419 (2002).
4. Jorge Lobo-Checa et al., Phys. Rev. Lett. **104**, 187602
5. K. Miyamoto et al., Phys. Rev. Lett. **108**, 066808 (2012).
6. Z. Hasan and C. L. Kane, Rev. Mod. Phys. **82**, 3045 (2010).
7. K. Miyamoto et al.,Phys. Rev. B **86**, 161411(R) (2012).
8. A. M. Shikin et al., Phys. Rev. Lett. **93**, 146802 (2004).

A systematic study on the interlayer electronic structure and electron-phonon coupling in the novel graphite intercalation superconductors

Chenlu Wang[1], Yan Zhang[1], Guodong Liu[1,*], Mingtian Zheng[2], M. Nakataki[2], K. Shimada[2] , Wenjuan Zhao[1], H. Namatame[2], M. Taniguchi[2] and Xingjiang Zhou[1,*]

[1]*National Laboratory for Superconductivity, Beijing National Laboratory for Condensed Matter Physics, Institute of Physics, Chinese Academy of Sciences, Beijing 100190, China*
[2]*Hiroshima Synchrotron Radiation Center, Hiroshima University, 2-313 Kagamiyama, Higashi-Hiroshima, Hiroshima 739-0046, Japan*

Keywords: graphite intercalation compounds (GICs), superconductors, ARPES.

Superconductivity in graphite intercalation compounds(GIC) is not fully understood yet. Basically, it is believed that the BCS mechanism arising from electron-phonon coupling (EPC) is responsible for pairing[1]. However, it needs to be clarified as which play a key role for the graphene sheet-derived π* bands and phonons, or the intercalant lattice-derived interlayer bands(IL) and soft phonons[2]. Up to now, there is no consensus on which one gives the dominant contribution[3-5]. It calls for a systematic research on the involved electronic states and a deep understanding on this issue. The solution is also important to the problem of superconductivity in graphene. The approved beam time in HiSOR were used to do Angle Resolved Photon Emission Spectroscope (ARPES) measurements on two typical GIC superconductors CaC_6 and KC_8.

In Fig. 1a and 1b, the unit cell and the in-plane atom projection are displayed for CaC_6. The guideline of hexagonal black pocket shown in Fig. 1c can be understood as a folding of the triangular graphene π* pockets owing to the super structure formed by Ca ordering as illustrated in Fig. 1b. So we can focus on two features in the BZ, one is the π* bands near the K region and the interlayer state and the folding bands at Gamma region.

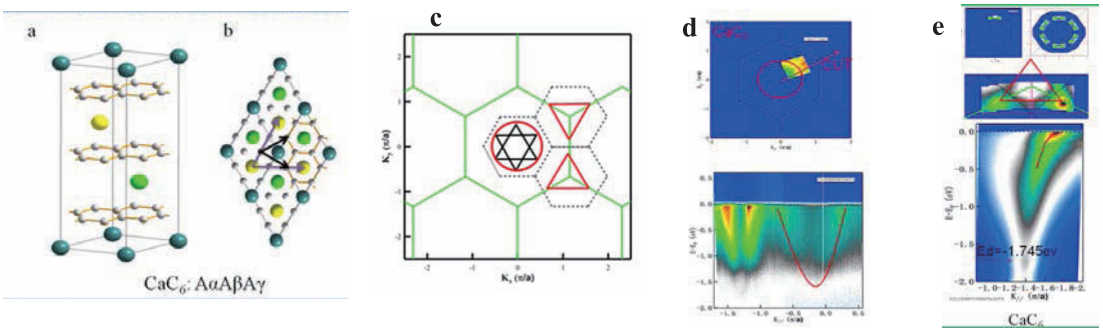

FIGURE 1. Electronic structure of CaC_6. (a) The crystal structure of CaC_6. (b) The atoms projection along the c-axis. The gray honeycomb lattice represents the graphene planes. The yellow, green, red and blue balls stand for the Ca atoms. Each colour corresponds to one certain layer. The black and purple arrows are the two-dimensional lattice vectors of the graphene lattice and the Ca super lattice, respectively. (c) The C (green) Brillouin zone (BZ) and the Ca-folded (dashed) BZ. The red triangles are electron-doped graphene π* pockets. The black triangles are the super lattice-folded π* pockets near Gamma point. The red circle marks is corresponds to the IL pocket. (d) The Fermi surface and band dispersion of CaC_6 in Gamma region. (e) The Fermi surface and band structure of CaC_6

First, we focus on the Gamma region. In CaC, a circular shaped Fermi surface and parabolic band dispersion is observed which account for the interlayer state, shown in Fig 1d. Apparently, there is no signal of the folding band. Then, let's check the K region. As shown in the Fig. 1e, clear bands and Fermi surface in K region were observed. Two “kinks” were found both at the center and corner of BZ, as demonstrated in Fig. 2. It is well known that a ‘‘kink’’ structure in the electronic dispersion and the concomitant change in the quasi-particle lifetime is the most prominent manifestation of electron phonon coupling at the energy scale of phonons. The direct observability of such effects in ARPES makes it an ideal tool to study EPC, particularly in anisotropic materials with EPC being significantly momentum dependent. The GICs are typical kinds of anisotropic materials.

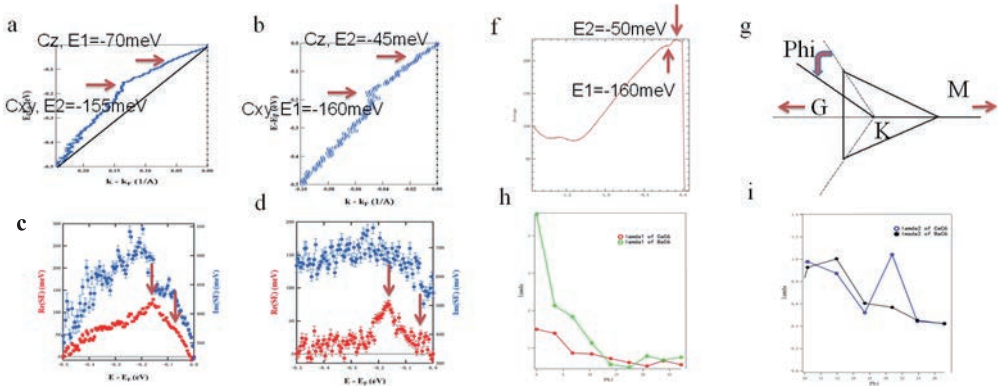

FIGURE 2. (a) and (b) Identification of electron–phonon modes in the dispersions for CaC_6 and BaC_6, respectively. (c) and (d) Extracted real and imaginary parts of the electronic self-energies of the π* bands for CaC_6 and BaC_6, respectively. (f) The sum of EDCs of π* bands for SrC_6 (g) Fermi surface shape in K region. Phi defines the polar angle around the K point, measured from the MK line. (h) and (i) The Electron-phonon Coupling strength constant VS polar angle as defined in (g). For comparison with CaC6, the data for BaC6 and SrC6 were collected in our lab-based ARPES system.

KC_8 is another interesting GIC superconductor, although with a rather low Tc=0.15K. The previous ARPES studies on this compound indicate that KC_8 can be regarded as potassium doped few layer graphene [6, 7]. But the recent research on CaC_6 [3] shows that the interstitial element form an interlayer band near Γ point, and the band is related to the superconductivity in this kind of material. Here we also discovered the parabola-like band around Γ point in KC_8. It indicated that the band is the interlayer band which might be related to KC_8’s superconductivity.

Figure 3 shows the lattice structure (a) and Fermi surface (b) which was measured in Hisor’s BL-7 ARPES system. Based on the K-folded BZ, we marked every pockets on the Fermi surface. Because there is no π* folding band in Γ point, we regard the circle like pocket as the interlayer pockets. Figure 4(b) shows a clear parabola like interlayer band. In KC_8, in principle, every unit cell distributes 0.25 potassium's electrons. While 0.11 potassium's electrons doped in graphite π* band[4]. Our circle map indicates that, the remanent 0.14 potassium's electrons should form a nearly free electron band --- interlayer band in Γ region. We also notice that KC_8’s interlayer band is quasi two-dimensional.

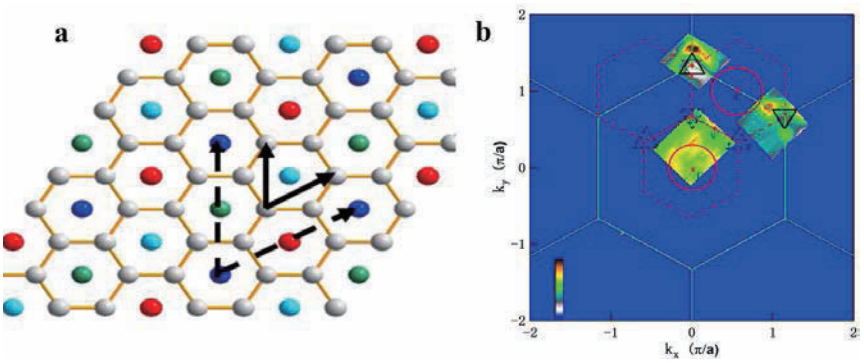

FIGURE 3. (a) KC_8 crystal structure viewed along the c-axis. The light grey balls represent the carbon atoms in graphite planes. The blue, light blue, red and green balls stand for the potassium atoms. Each color corresponds to one

potassium layer. The solid and dashed arrows are the two-dimensional lattice vectors of the one layer graphite lattice and the potassium superlattice, respectively. (b) Fermi surface map plotted in both the C2 (solid green lines) Brillouin zone (BZ) and the K-folded (dashed red lines) BZ, The solid black triangles are representations of the electron-doped graphene π* pockets, The dashed black triangles illustrate the superlattice-folded π* pockets near Γ. The dashed red circle marks the interlayer pockets.

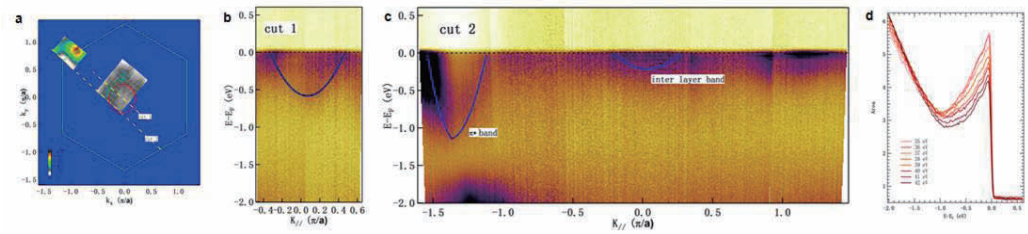

FIGURE 4. (a) Fermi surface map measured with 43 eV photon energy, a clear circle (red solid circle) map near Γ point. (b) The measured band structure along cut 1. The solid bule line represents the nearly free electron band fitted by quadratic function. (c) The original measured band structure along cut 2. We can see π* and interlayer band clearly. (d) Integral spectrum cross Γ point measured from 35 eV to 42 eV photons. It indicates that the KC8's interlayer band has little dispertion along Kz.

In summary, we took much efforts to obtain high quality graphite crystals and succeeded by ourselves in synthesizing CaC_6(Tc=11.5K), SrC_6 (Tc=1.65K), KC_8 (Tc=0.15 K) and BaC_6 (non-superconducting) single crystal samples with excellent phase purity. These GICs were systematically measured by the synchrotron radiation-based ARPES and also our lab-based ARPES. From our results, for CaC_6, we found that the π* bands show two kinks: one is located at 150-200 meV, coupling with Cxy phonon mode; and another at 40-90 meV, coupling with Cz phonon mode. It indicates that the EPC is very anisotropic. In the Brilloin zone center, we identified the interlayer band in both CaC_6 and KC_8. Different from the CaC_6 interlayer band [5], the interlayer band in KC_8 has little K_z dispersion. The interlayer band might be related to the superconductivity in KC_8 as well. Therefore, we could speculate that the interlayer band might play an key role for the superconductivity in all GICs.

REFERENCES

1. N. Emery et. al, PRL 95, 087003 (2005)
2. G. Csanyi et. al, nphys119 (2005)
3. T. Takahashi et.al, nphys 1128 (2008)
4. T. Valla et.al, PRL 102, 107007 (2009)
5. S.-L. Yang, et al. ncomms4493 (2014)
6. A. Grüneis et al., *Phys. Rev. B* **79**, 205106 (2009).
7. A. Grüneis et al., *Phys. Rev. B* **80**, 075431 (2009)
8. Pan, Z.-H. *et al*. *Phys. Rev. Letters* **106**, 187002 (2011).

Fermi surface of heavy-fermion compound $EuNi_2P_2$ revealed by angle-resolved photoemission spectroscopy

H. Anzai[a], K. Ichiki[a], E. F. Schwier[b], H. Iwasawa[b], M. Arita[b], K. Shimada[b], H. Namatame[b], M. Taniguchi[b], A. Mitsuda[c], H. Wada[c], and K. Mimura[a,b]

[a] *Graduate School of Engineering, Osaka Prefecture University, Sakai 599-8531, Japan*
[b] *Hiroshima Synchrotron Radiation Center (HSRC), Hiroshima University, Higashi-Hiroshima 739-0046, Japan*
[c] *Graduate School of Science, Kyushu University, Fukuoka 819-0395, Japan*

Keywords: Heavy Fermion behavior, Eu compound, angle-resolved photoemission spectroscopy.

In rare-earth compounds, the hybridization between conduction and localized-*f* electrons (*c*-*f* hybridization) leads to the formation of a strongly renormalized quasiparticle, and it is the major contributor to the possible mechanisms for the heavy-fermion state. $EuNi_2P_2$ is known as the first heavy-fermion compound among Eu-based materials, with an electronic specific heat coefficient $\gamma \sim 100$ mJ / (K^2·mol) [1]. The mean valence of Eu ions deduced from the Mössbauer isomer shift varies significantly from 2.25 at 300 K to 2.50 at 1 K [2]. In reality, the conduction electron mediates the electron transfer between the two Eu states. To understand these unique physical properties in $EuNi_2P_2$, the experimental data from an electron point of view are required.

Angle-resolved photoemission spectroscopy (ARPES) is a direct probe to measure the electronic excitation as functions of energy and momentum. A previous ARPES study of $EuNi_2P_2$ reported that the electronic structure near the Fermi level (E_F) consists of multiple bands and orbitals [3]. Furthermore, an energy gap due to hybridization between the Ni 3*d* and Eu 4*f* states was observed at $|\omega| \sim 0.6$ eV. These results indicate that multiband electronic structure and the hybridization effect are key to the physics of the heavy-fermion behavior. However, the details of the Fermi surface topology remain unexplored.

Here, we report an ARPES study of the Fermi surface in $EuNi_2P_2$ by using linearly polarized incident synchrotron radiation. We revealed that three bands intersect E_F and form complicated Fermi surface topology. The ARPES measurements were performed at BL-1 and BL-9A of Hiroshima Synchrotron Radiation Center, where two linearly polarized lights (*s*- and *p*-polarized photons) are achieved. The data were taken with 8 ~ 70 eV photons. The total energy resolution was set to 25 meV. The samples were cleaved *in situ* and kept under ultrahigh vacuum better than 5×10^{-11} Torr.

The momentum distribution curves (MDCs) taken with the *s*-polarized photons along the Γ-X direction are shown in Fig. 1(b). A weak but resolvable band (labeled as α) is observed at $|\omega| \sim 0.45$ eV and crosses E_F. This

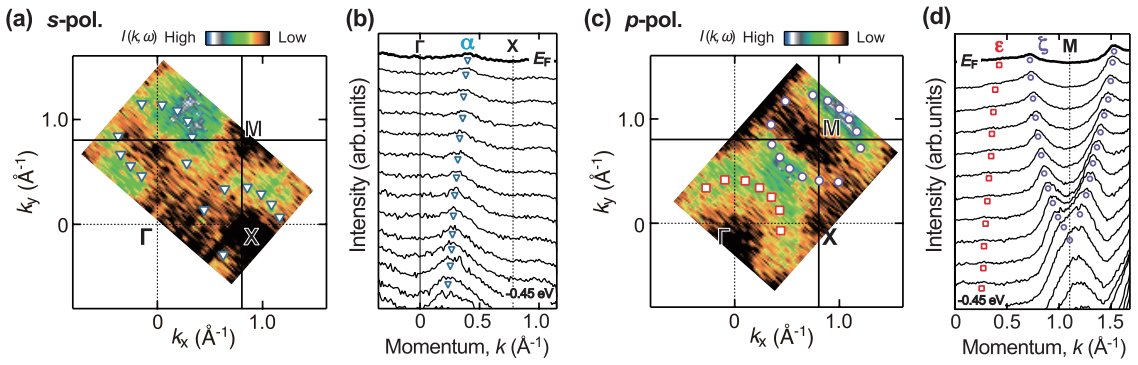

Figure 1. (**a**) Photoemission intensity map obtained by integrating the intensities over an energy range of $E_F < |\omega| < 0.2$ eV. The data are taken with *s*-polarized 70 eV photons. Blue triangles are Fermi momentum, k_F, obtained by tracking the Fermi-level crossings in the momentum distribution curves (MDCs). (**b**) MDCs along the Γ-X direction. (**c**) The same as panel (a) but taken with the *p*-polarized photons. Red triangles and purple circles are the k_F. (**d**) MDCs along the Γ-M direction.

band forms a hole-like Fermi pocket around X point, as demonstrated by the photoemission intensity map in Fig. 1(a). We found that the shape of the Fermi surface dramatically changes with the polarization of the incident radiation. The data taken with *p*-polarized photons are displayed in Figs. 1(c) and (d). The spectral intensity now surrounds the Γ and M points, as shown in Fig. 1(c). Two bands (labeled as ε and ζ) intersect E_F along the Γ-M direction. The ε band encloses the Γ point, forming the circle-shaped electron pocket. The parabolic ζ band, whose band bottom is at $|\omega| \sim 0.4$ eV below E_F, forms electron Fermi pockets around the M point.

The observed Fermi surfaces are well nested along the (π, π) direction. The scattering of electrons between the nested Fermi surfaces effectively drives the system into an ordered ground state. As a result, an energy gap opens at E_F. In our experiments, no energy gap related to Fermi surface nesting was observed. However, the existence of some kind of gap near E_F, such as the *c*-*f* hybridization gap and charge-density-wave gap, may provide a natural explanation for the mass enhancement, involving the heavy-fermion state in $EuNi_2P_2$. Further experiments under high energy and momentum resolutions are necessary to confirm the energy gap.

In conclusion, we have studied Fermi surface of $EuNi_2P_2$ by ARPES. There are three bands intersecting the Fermi level, which form one hole pocket and two electron pockets around the X, Γ, and M points, respectively. It is clear that there are some nested Fermi segments in this multiband electronic structure. Our results suggest that the Fermi surface nesting is related to the mechanisms for the heavy fermion state in $EuNi_2P_2$.

References

[1] R. A. Fisher *et al*., Phys. Rev. B **52**, 13519 (1995).
[2] R. Nagarajan *et al*., Phys. Rev. B **32**, 2846 (1985).
[3] S. Danzenbächer *et al*., Phys. Rev. Lett. **102**, 026403 (2009).

Angle-resolved Photoelectron Spectroscopy Study of $Ce(Ru_{1-x}Rh_x)_2Al_{10}$

H. Yamaoka[a], E. F. Schwier[b], Y. Yamamoto[c], F. Tajima[d], T. Nishioka[d], H. Iwasawa[b], K. Shimada[b], and J. Mizuki[c],

[a]*RIKEN SPring-8 Center, Sayo, Hyogo 679-5148, Japan*
[c]*Hiroshima Synchrotron Radiation Center, Hiroshima University, Higashi-Hiroshima, Hiroshima 739-0046, Japan*
[b]*Graduate School of Science and Technology, Kwansei Gakuin University, Sanda, Hyogo 669-1337, Japan*
[d]*Graduate School of Science, Kochi University, 2-5-1 Akebono, Kochi 780-8520, Japan*

Keywords: electronic structure, photoelectron spectroscopy, Ce1-2-10, DFT calculations

The ternary intermetallic compounds RT_2Al_{10}, where R is a rare earth and T one of the transition metals Ru, Os, or Fe, were discovered by Thiede *et al.* in 1998 [1-3]. In CeT_2Al_{10} antiferromagnetic (AFM) order occurs for T = Ru and Os at unusually high ordering temperatures (T_0 = 27.3 K and 28.7 K). The long Ce-Ce distances of > 5Å in CeRu2Al10 and CeOs2Al10 and de-Gennes scaling imply ordering temperatures below a few K, so that conventional RKKY interaction can be ruled out as the origin of the magnetic order. Furthermore, the direction of the ordered moments comes as a surprise since it is aligned along the c axis and not along the easy axis a. It was suggested that the c-f hybridization is strongest along the a axis, leading to an easy magnetization axis in the c (a?) direction. Macroscopic properties of Ce1-2-10 systems have been studied in detail. However, no angle-resolved photoelectron spectroscopy (ARPES) has been reported so far. Information of detailed electronic structure is a key to understand unconventional physical properties described above.

At the SPring-8, we performed x-ray emission spectroscopy of $Ce(Ru_{1-x}Rh_x)_2Al_{10}$, which may show a Lifshitz transition between x = 0.03 and 0.05, where the electronic structure is expected to change largely without a structural phase transition [4, 5]. X-ray absorption spectra with partial fluorescence mode showed that there is sudden increase of f^0 intensity, i. e. the increase of the c-f hybridization strength, between x = 0.03 and 0.05. Hard x-ray PES at BL12XU, SPring-8 also showed a similar result.

In this report, we show the combined PES and ARPES results of $Ce(Ru_{1-x}Rh_x)_2Al_{10}$ obtained at HiSOR. Figure 1 shows the Laser PES result of the valence band spectra near the Fermi level of the x = 0.03 and 0.05 samples. Similar high-resolution spectra have been observed in CeT_2Al_{10} (T = Ru, Fe, Os) with using the light from the Xe lamp [6]. There is a large difference of the density of states at the Fermi level between two samples. The result indicated that the hybridization strength of the x = 0.05 sample may be much larger compared to that of the x = 0.03 sample. It should be noted that the spectra were obtained using a light spot of the order of a few microns in diameter. This allowed us to scan the surface of the cleaved crystal and search for the sharpest Fermi edge, which in turn we attribute to the most representative surface.

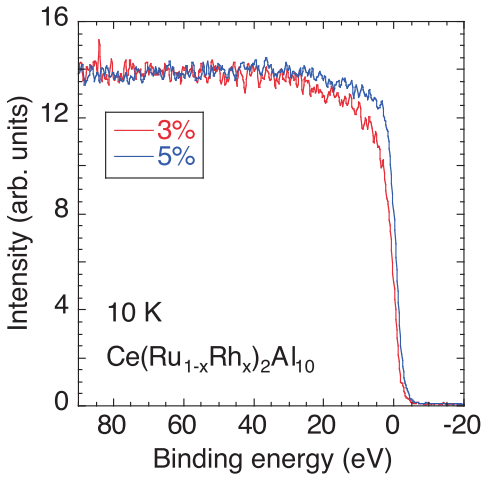

FIGURE 1. Valence band spectra of $Ce(Ru_{1-x}Rh_x)_2Al_{10}$ (x = 0.03, 0.05) near the Fermi level at 10 K.

In Fig. 2 we show the ARPES results of the x = 0 sample measured at $h\nu$ = 115 eV compared with DFT calculations. Due to the large unit cell, the number of bands is very large and it is more illustrative to plot the orbital weight (in this case of the Ce d) to compare the DFT results with the ARPES spectra. Even though the background in the ARPES is comparatively large to the signal intensity, it is possible to identify the main feature in the DFT at a binding energy of -0.75 eV. This demonstrates that for the valence band in general a simple DFT approach may be sufficient to describe the electronic structure.

Because of the large difference of the electronic structure between x = 0 (0.03) and x = 0.05, we analyze further if the DFT can reproduce significant changes in the electronic structure close to the Fermi energy, by introducing an electron doping in the unit cell. In Figure 3 we plot the band dispersion close the Fermi level for the undoped (red) and the x = 0.05 doping case (black). We shifted the doped bands 40 meV towards higher energies to match most of the bands with each other and account for an electron doping in a rigid band picture.

Overall the band structures match well after the artificial shift is included. However, upon further inspection we can see that the bands at the Γ and Z (and to a smaller degree the X and Y) points are mismatched. This change of the bands binding energies shows a deviation from the rigid band model and may be seen as a signature of orbital hybridization at the Fermi level. This hybridization as well as the number of bands crossing the Fermi level may be the reason of the transition between the x = 0 (0.03) and x = 0.05 samples. Further theoretical analysis incorporating correlation effects may answer this question.

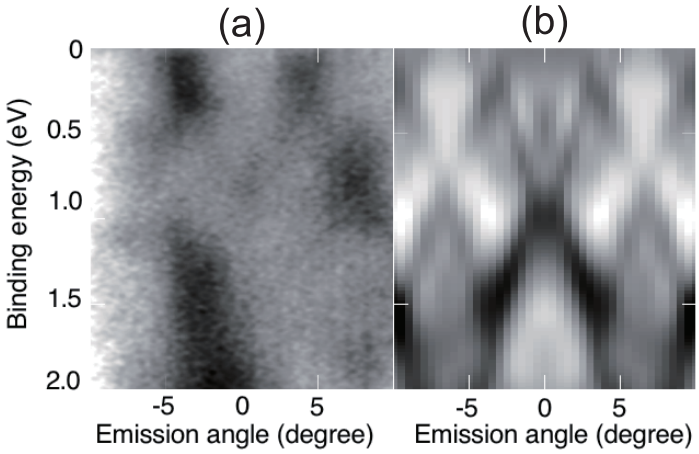

FIGURE 2. Band dispersion of $CeRu_2Al_{10}$ (x = 0). (a) Experimental result measured at $h\nu$ = 115 eV. (b) DFT calculation result of $CeRu_2Al_{10}$.

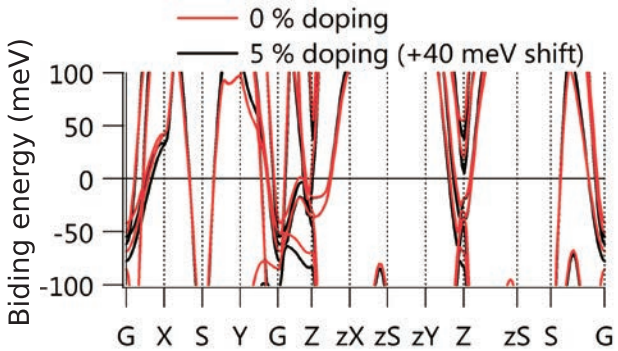

FIGURE 3. DFT calculated result: Band dispersion near the Fermi level of $Ce(Ru_{1-x}Rh_x)_2Al_{10}$ (x = 0 (red line), 0.05 (black line)). Note that the energy of the x = 0.05 sample was shifted.

References

1. V. M. T. Thiede, T. Ebel, and W. Jeitschko, J. Mater. Chem. **8**, 125 (1998).
2. T. Nishioka, Y. Kawamura, T. Takesaka, R. Kobayashi, H. Kato, M. Matsumura, K. Kodama, K. Matsubayashi, and Y. Uwatoko, J. Phys. Soc. Jpn. **78**, 123705 (2009).
3. Y. Zekko, Y. Yamamoto, H. Yamaoka, F. Tajima, T. Nishioka, F. Strigari, A. Severing, J.-F. Lin, N. Hiraoka, H. Ishii, K.-D. Tsuei, and J. Mizuki, Phys. Rev. B **89**, 125108 (2014).
4. H. Tanida, H. Nohara,M. Sera, T. Nishioka,M.Matsumura, andR. Kobayashi, Phys. Rev. B **90**, 165124 (2014).
5. S. Kimura, H. Tanida, M. Sera, Y. Muro, T. Takabatake,. T. Nishioka, M. Matsumura, and R. Kobayashi, Phys. Rev. B **91**, 241120 (2015).
6. T. Ishiga, T. Wakita, R. Yoshida, H. Okazaki, K. Tsubota, M. Sunagawa, K. Uenaka, K. Okada, H. Kumigashira, M. Oshima, K. Yutani, Y. Muro, T. Takabatake, Y. Muraoka, and T. Yokoya, J. Phys. Soc. Jpn. **83**, 094717 (2014).

ARPES research of a possible weyl semimetal material

Jianwei Huang[a] Aiji Liang[a] Qiang Gao[a] Shaolong He[a], Mingtian Zheng[b], E. F. Schwier[b], H. Iwasawa[b], H. Sato[b], K. Shimada[b], H. Namatame[b], and Xingjiang Zhou[a]

[a] *Beijing National Laboratory for Condensed Matter Physics, Institute of Physics, Chinese Academy of Sciences, Beijing 100190, China*
[b] *Hiroshima Synchrotron Radiation Center Hiroshima University 2-313 Kagamiyama, Higashi-Hiroshima City, 739-0046 JAPAN*

Keywords: ARPES, SrMnSb2, Electronic structures

Quantum topological materials have been a very hot topic recently because of its possible applications and the concepts grafted from high energy physics into condensed matter physics. Recently, the Weyl semimetal has attracted researcher's interest with its low energy excitation behaves as Weyl Fermion. A new family of space-inversion-symmetry-breaking Weyl semimetal has been found theoretically and experimentally(TaAs, TaP, NbAs, NbP)[1-5]. Another kind of Weyl semimetal which is realized by time-reversal-symmetry-breaking has also been predicted by theory but not observed directed by experiment. Very recently a new material $SrMnSb_2$ has been reported to exist relativistic Fermion property coexist with ferromagnetic behavior[6,7]. It has a great opportunity to be a time-reversal-symmetry-breaking Weyl semimetal.

Angle-resolved photoemission spectroscopy (ARPES) is a powerful tool to study electronic structure of different kinds of materials due to its combination of energy-momentum resolved abilities and surface sensitivity. Here we report ARPES results on $SrMnSb_2$ obtained at beamline BL-7 and BL-1 in Hiroshima Synchrotron Radiation Center. Single crystals of $SrMnSb_2$ were cleaved in (100) surface. We did a quick mapping of the sample and photon energy dependent high symmetry cuts in the second Brillouin zone. We found the electronic structure agrees well with our HeI measurements and exhibits strong 2D property. Further experiments still need to be done to investigate its topological properties.

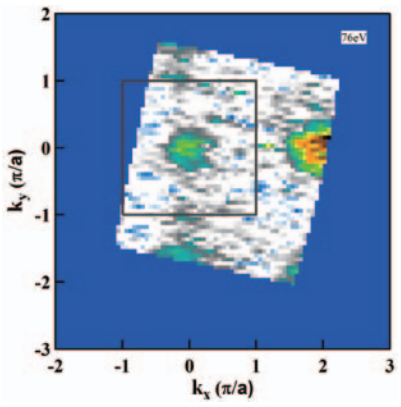

FIGURE 1. Fermi surface of $SrMnSb_2$ Fermi Surface mapped by using 76 eV photon. One hole pocket near Gamma and two point-like Fermi Surface near Brillouin zone boundary are observed. The grey square line is a indication for the first Brillouin zone.

Fig. 1 is Fermi Surface map of $SrMnSb_2$ using 76eV photon. The data was integrated within 20 meV to improve statistics. The Fermi Surface consists of hole pocket at Gamma point and point-like FS at Y point. The point-like Fermi surface is hole-like according to the band dispersion in Fig. 2.

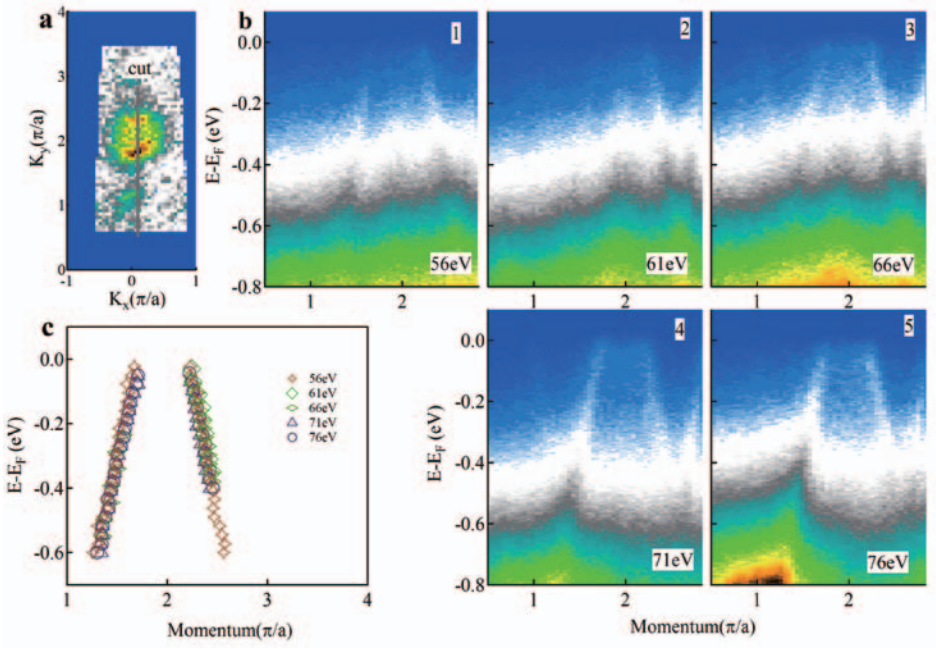

FIGURE 2. Photon energy dependent band dispersion along Y-Gamma-Y direction in the second Brillouin zone. (a) Fermi Surface in the second Brillouin zone, the grey line indicate cut location in (b). (b1-b5) Intensity distribution of cut in (a) with photon energies of 56eV, 61eV, 66eV, 71eV, 76eV. (c) A fit of band dispersions in (b).

Figure 2 is the band dispersion we got using different photon energies along Y-Gamma-Y direction. A fit of the band dispersion around Gamma point can be found in Fig2c. These band dispersions present linear property over a quite wide energy range up to -0.8eV which means these electrons are almost massless. Moreover these bands overlap with each other quite well. One explanation is SrMnSb2 has strong 2D electronic structure. Another explanation is the hole-like band around Gamma is surface state of SrMnSb2. Further experiments need to be done to pin down whether it is bulk band or surface state.

REFERENCES

1. S. M. Huang et al., A Weyl Fermion semimetal with surface Fermi arcs in the transition metal monopnictide TaAs class. Nat. Commun. 6, 7373 (2015).
2. H. M. Weng et al., Weyl semimetal phase in noncentrosymmetric transition-metal monophos-phides. Phys. Rev. X 5, 011029 (2015).
3. S. Y. Xu et al., Discovery of a Weyl fermion semimetal and topological Fermi arcs. Science 349, 613 (2015).
4. B. Q. Lv et al., Experimental discovery of Weyl semimetal TaAs. Phys. Rev. X 5, 031013 (2015).
5. L. X. Yang et al., Weyl semimetal phase in the non-centrosymmetric compound TaAs. Nature Physics 11. 9 (2015).
6. J.Y. Liu et al., Discovery of a topological semimetal phase coexisting with ferromagnetic behavior in Sr1-yMnSb2 (y~0.08). arXiv: 1507.07978
7. Farhan, M. A et al., AEMnSb2 (AE=Sr, Ba): a new class of Dirac materials. Journal of Physics: Condensed Matter 26, 042201, (2014).

A study on thermal reaction with sulfenamide as vulcanization accelerator by means of S K-edge NEXAFS

S. Tanaka[a], C. Tsukada[d], S. Ogawa[a,c], G. Kutluk[b], T. Murai[c] and S. Yagi[b,c,d]

[a] *Graduate School of Engineering, Nagoya University, Japan*
[b] *Hiroshima Synchrotron Radiation Center, Hiroshima University, Japan*
[c] *Aichi Synchrotron Radiation Center, Aichi Science & Technology Foundation, Japan*
[d] *Institute of Materials and Systems for Sustainability, Nagoya University, Japan*

Keywords: Rubber, Vulcanization, Vulcanization accelerator, Sulfenamide, S K-edge NEXAFS, He-path system

Rubber products are widely used in our life because they have high properties of the restorative force and the retractility. Those products are fabricated by mixing a raw rubber and a sulfur (S_8) at 140~160 °C. The fabricated rubbers have cross-linked structures. The cross-linked structure is formed by the bonding between the atomic chain of S_8 and the molecular chain of raw rubber [1]. This reaction is called as vulcanization. The vulcanization takes a long time. If the rubber is industrially fabricated, the vulcanization should be completed in a short time. The requirement is accomplished by adding vulcanization accelerators [2]. In this study, we focus on the sulfenamide, which is one of the vulcanization accelerators. The sulfenamide is the most useful vulcanization accelerator in the industry. The rubber with sulfenamide possesses a good physical performance. In addition, the vulcanization reaction of the rubber with sulfenamide is stable because the reaction has an induction period. However, the detail of the reaction of the rubber with sulfenamide is almost unclear. M.H.S. GRADWELL *et al.* have speculated that the scission of S-N bond for sulfenamide initially occurs when the reaction is promoted [3]. The scission reaction is regarded as thermal decomposition reaction. They could not analyze a change of chemical bonding state in thermal decomposition reaction. On the other hand, we can analyze the chemical bonding state of sulfur element using S K-edge NEXAFS measurement. The purpose in this study is to reveal the thermal decomposition reaction of sulfenamide by means of S K-edge NEXAFS measurement.

We selected N-cyclohexylbenzothiazole sulfenamide(CBS) as the sample powder. CBS is one of sulfenamide. S K-edge NEXAFS measurements were carried out by fluorescence X-ray yield mode using the atmospheric XAFS measurement system with He-path [4] at both HiSOR BL-3 and AichiSR BL6N1, respectively. The spectrum of CBS at room temperature was obtained at HiSOR. The cell of *in-situ* NEXAFS measurement was made by using polyimide film (Kapton). CBS was injected into the cell. *in-situ* S K-edge NEXAFS measurement for CBS during heating was carried out at AichiSR. The photon energy was calibrated to the peak position of K_2SO_4 at 2481.7 eV.

FIGURE 1 shows S K-edge NEXAFS spectra for CBS at room temperature, 210 °C and 230 °C, respectively. For the spectrum at room temperature, the shoulder structure is observed around 2473.8 eV. This shoulder structure shows the existence of the S-N bonds. The spectrum at 210 °C has the small shoulder structure around 2473.8 eV and the new shoulder structure around 2471.8 eV in comparison with that at room temperature. The shoulder structure around 2471.8 eV shows the existence of the S-S bonds. The number of S-N bonds is decreased and the number of S-S bonds is increased when CBS is heated at 210 °C. It is found that the thermal decomposition reaction of CBS starts at 210 °C. The spectrum at 230 °C has the small shoulder structure around 2471.8 eV and the new peak around 2475.3 eV in comparison with that at 210 °C. The peak around 2475.3 eV shows the existence of the S-H bonds. The number of S-S bonds is decreased and the number of S-H bonds is increased at 210~230 °C . Considering those results, we propose the reaction model shown in FIGURE 2. We conclude that CBS transforms into MBTS at 210 °C. Subsequently MBTS transforms into MBT at 210~230 °C. The thermal decomposition reaction of CBS has two stage processes.

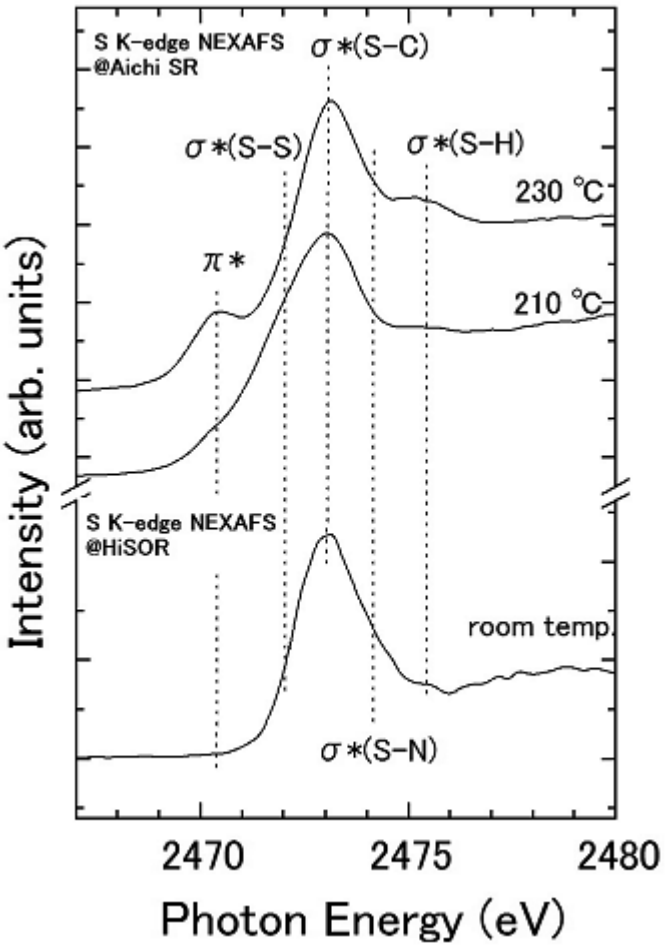

FIGURE 1. S K-edge NEXAFS spectra for CBS at room temperature, 210 °C and 230 °C, respectively.

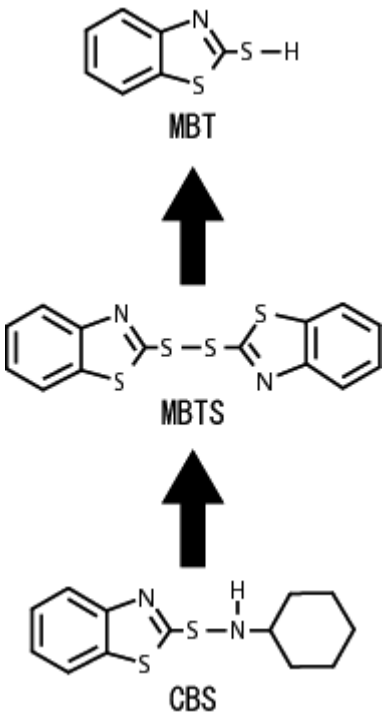

FIGURE 2. Thermal decomposition reaction model of CBS.

REFERENCES

1. Nippon Gomu Kyokai : "*Gomu Gijutu no Kiso*" P.1 (2014).
2. T. Komatsu, *Nippon Gomu Kyokaishi,* **82**, 33 (2009).
3. M. H. S. GRADWELL and W. J. MCCILL, *J. Appl. Polym.Sci.*, **51**, 169 (1994). 4. S. Yagi, Y. Matumura, K. Soda, E. Hashimoto, M. Taniguchi, *Surf. Interface Anal.* **36**, 1064 (2004).

Adsorption behavior between L-cysteine and Au nanoparticles precovered with different order of PC layer

C. Tsukada[a], K. Matsuo[b], T. Murai[c], T. Nomoto[d],G. Kutluk[b], H. Namatame[b], M. Taniguchi[b], T. Yaji[e], T. Ohta[e], H. Nameki[d], S. Ogawa[c,f] and S. Yagi[a,b,c,e]

[a] *Institute of Materials and Systems for Sustainability, Nagoya University, Japan*
[b] *Hiroshima Synchrotron Radiation Center, Hiroshima University, Japan*
[c] *Aichi Synchrotron Radiation Center, Aichi Science & Technology Foundation, Japan*
[d] *Aichi Center for Industry and Science Technology, Aichi Prefecture, Japan*
[e] *The SR Center, Ritsumeikan University, Japan*
[f] *Graduate School of Engineering, Nagoya University, Japan*

Keywords: Au nanoparticles, Different order of phosphatidylcholine (PC) layer, L-cysteine, Adsorption reaction, S K-edge NEXAFS, He-path system, Infrared spectroscopy

Gold nanoparticles (AuNPs) are expected to apply to the hyperthermia for cancer cell in medical field [1]. The AuNPs are hoped to possess the high biocompatibility. We propose a hypothesis that if a biomolecule is not easy to adsorb on the AuNPs surface, the NPs have high biocompatibility. In our previous study, the L-cysteine has adsorbed rapidly on the AuNPs [2], which are fabricated by the solution plasma method reported by H. Nameki [3]. We speculate that the L-cysteine adsorption can be inhibited with forming the AuNPs precovered with the ordered layer like a self-assembled monolayer. Thus, we have fabricated the AuNPs precovered with the ordered phosphatidylcholine (PC) layer, which are described as "PC/AuNPs" [4]. The PC has been extracted from egg. The PC layer has formed by both the adsorption of PC on AuNPs surface at hydrophilic groups and the occurrence of intermolecular force between hydrocarbon chains of hydrophobic groups of the PC.

Subsequently, we take notice of the different types of the hydrocarbon chain of PC. M.D. Porter *et al.* have reported that the layer structure of alkyl thiol on gold becomes increasingly disordered with lower packing density and coverage, when the chain length decreases [5]. We have revealed that the PC layer with unsaturated bond becomes disordered compared to that without unsaturated bond [6]. In this study, therefore, if there are the changes of the length of hydrocarbon chain of PC and/or the existence of unsaturated bond, we think that the L-cysteine adsorption states on the PC/AuNPs also become different. The purpose in this study is to reveal the adsorption reaction between the L-cysteine and the AuNPs precovered with different order of PC layer by means of sulfur K-edge near-edge X-ray absorption fine structure (S K-edge NEXAFS) and infrared microspectroscopy (IR) measurements.

The AuNPs colloidal solution was fabricated by the solution plasma method [3]. The method used gold rods and NaCl aqueous solution. The hydrocarbon chain of diheptanoyl PC (DHPC) has 7 carbons without unsaturated bond. The each solution (DHPC aqueous solution, AuNPs colloidal solution, ascorbic acid aqueous solution and $HAuCl_4$ aqueous solution) was added into milli-Q water with stirring at room temperature. The Au^{3+} ions were reduced around AuNPs and the large NPs, which were described as "DHPC/AuNPs", were obtained. The L-cysteine was added into the DHPC/AuNPs solution. After promoting the adsorption reaction, the occurred precipitate was rinsed several times with milli-Q water. This precipitate was dropped on the kapton film and dried in air. This sample is called as "Cysteine/DHPC/AuNPs". The hydrocarbon chain of dipalmitoyl PC (DPPC) has 16 carbons without unsaturated bond. The DPPC aqueous solution was kept at 45°C and was added into the AuNPs colloidal solution. The occurred precipitate, which was the DPPC/AuNPs, was taken up and rinsed several times with milli-Q water. The L-cysteine was added into the aqueous solution with precipitate. After promoting the adsorption reaction, the precipitate was rinsed with the milli-Q water again. This precipitate was dried in the polyethylene bubble wrap. This sample is called as "Cysteine/DPPC/AuNPs".

S K-edge NEXAFS measurements with He-path system [7] were carried out at HiSOR BL-3 using proportional counter and AichiSR BL6N1 using silicon drift detector, respectively. IR measurement was carried out at the SR center BL-15 in Ritsumeikan University.

FIGURE 1 shows the S K-edge NEXAFS spectra for the Cysteine/DHPC/AuNPs measured at both HiSOR and AichiSR. Those spectra are superimposed. The L-cysteine powder spectrum is also shown as a standard. The profile of Cysteine/DHPC/AuNPs spectrum at HiSOR indicates the gradually intensity increase according to increasing photon energy. This intensity increase may derive from scattered X-ray. On the other hand, those profiles of Cysteine/DHPC/AuNPs spectra around 2463~2474 eV have similar structure. The shoulder structure around 2471.0 eV and the peak at 2473.5 eV are observed, respectively. The shoulder structure shows the existence of atomic S on AuNPs, which occurs by dissociating of S-H and S-C bonds of the L-cysteine. The peak may show that the L-cysteine adsorbs on the AuNPs surface at SH group and subsequently the S-H bond dissociates. It is because the peak is assigned to σ*(S-C) and exists higher energy position compared to the peak of L-cysteine powder at 2472.7 eV assigned to σ*(S-C) [8].

The Cysteine/DPPC/AuNPs spectrum, not shown here, has the small shoulder structure around 2471.0 eV and the new peak at 2481.7 eV in comparison with the Cysteine/DHPC/AuNPs spectrum. The length of hydrocarbon chain of DHPC is shorter than that of DPPC. M.D. Porter *et al.* have reported that when the chain length of alkyl thiol decreases, the layer structure on gold becomes increasingly disordered with lower packing density and coverage [5]. Therefore, in our study, we think that the L-cysteine can be easy to adsorb on the AuNPs surface of DHPC/AuNPs compared to DPPC/AuNPs. As the result, the intensity of shoulder structure around 2471.0 eV of Cysteine/DHPC/AuNPs is larger than that of Cysteine/DPPC/AuNPs. On the other hand, because the DPPC has 16 carbons without unsaturated bond, each existence position of the functional groups of DPPC molecules on AuNPs becomes close. In addition, IR data, not shown here, indicate the possibility of bonding with the SH group of L-cysteine and the O=C group of DPPC. Thus, we think that the new peak at 2481.7 eV of Cysteine/DPPC/AuNPs indicates the SO_4 formed by the SH group and the O=C group. The adsorption reaction model is shown in FIGURE 2.

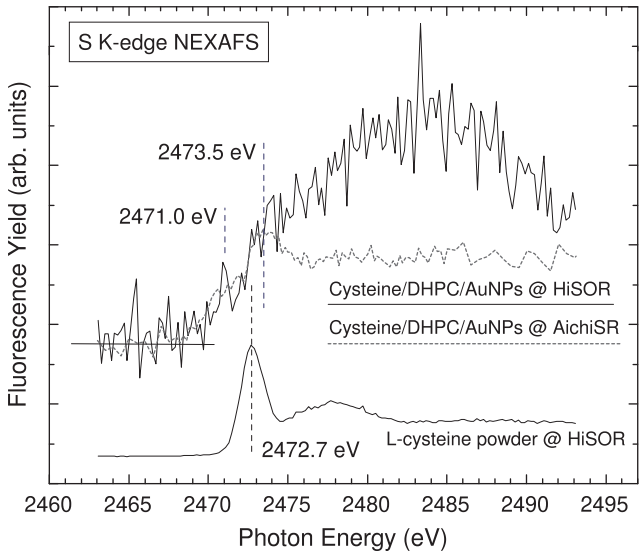

FIGURE 1. S K-edge NEXAFS spectra for Cysteine/DHPC/AuNPs and L-cysteine powder.

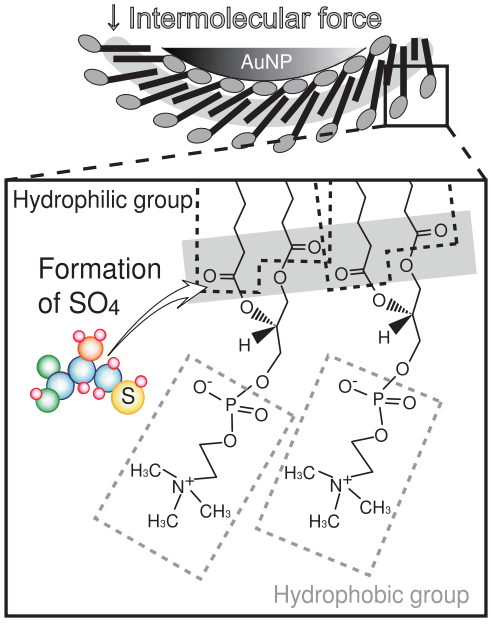

FIGURE 2. Adsorption reaction model of Cysteine/DPPC/AuNPs.

REFERENCES

1. H.-C. Huang, K. Rege, J.J. Heys, *ACS Nano* **4**, 2892-2900 (2010).
2. C. Tsukada, T. Mizutani, S. Ogawa, T. Nomoto, Y. Abe, H. Nameki, K. Matsuo, G. Kutluk, S. Yagi, *e-J. Surf. Sci. Nanotech.* **11**, 18-24 (2013).
3. H. Nameki, "Trial-Core ~Effort of plasma technique for industrial application in Aichi Prefecture~" 2013; http://www.aichi-inst.jp/sangyou/up_docs/hyoumen_trialdetail.pdf
4. C. Tsukada, "Study on adsorption reaction between Au nanoparticle and biomolecules toward administration to living body", Ph.D. Thesis, Nagoya University, 2015.
5. M.D. Porter, T.B. Bright, D.L. Allara, C.E.D. Chidsey, *J. Am. Chem. Soc.* **109**, 3559-3568 (1987).
6. C. Tsukada, T. Tsuji, K. Matsuo, T. Nomoto, T. Muai, T. Yaji, T. Ohta, H. Nameki, S. Ogawa, T. Yoshida, S. Yagi, presents in international conference of 27th European Conference on Biomaterials (2015).
7. S. Yagi, Y. Matsumura, K. Soda, E. Hashimoto, M. Taniguchi, *Surf. Interface Anal.* **36**, 1064-1066 (2004).
8. P. Zhang, T.K. Sham, *Phys. Rev. Lett.* 90, 245502 1-4 (2003).

Current activities of research and education on BL-5

T. Yokoya, T. Wakita, and Y. Muraoka

Graduate School of Natural Science and Technology, Okayama University

Keywords: photoemission spectroscopy, photoelectron emission microscopy

We present an overview of our resent research and educational activities on beamline 5 (BL5). Our beamline has two experimental stations in a tandem way. The first station is equipped with an angle-resolved photoemission spectrometer (ARPES), a low energy electron diffraction (LEED) apparatus and an X-ray source. The hemispherical analyzer of ARPES spectrometer (HA54, VSW) has a mean radius of 50 mm and is mounted on a twin axis goniometer in ultra-high vacuum chamber. Using this goniometer, one can perform ARPES and photoelectron diffraction (PED) measurements. It is also possible to perform resonant photoemission spectroscopy (RPES) measurements by using photon energy tunability of synchrotron radiation with X-ray absorption spectroscopy (XAS) measurement. With the X-ray source (XR2E2, FISONS), we can perform an X-ray photoelectron spectroscopy (XPS) measurement for the chemical state analysis and the PED. At the second station, we have installed a photoelectron emission microscope (PEEM, 'PEEM III', Elmitec). PEEM provides a magnified image of lateral intensity distribution of photo-emitted electrons from a sample surface. The spatial resolutions are several ten nanometers with Hg lamp and a few micrometers with synchrotron radiation. The sample is transferred between the ARPES and the PEEM chamber *in-situ*, and one can perform measurements at both stations for the same sample.

In the recent researches on BL-5, we have studied the electronic structure of potassium doped aromatic molecule (K_x picene) [1], iron-based superconductor ($FeSe_xTe_{1-x}$) [2], transition metal di-oxide films such as VO_2 thin films which exhibits a first-order metal-to-insulator transition at 340 K [3], CrO_2 thin films which are known as a half-metallic material [4], and TaO_2 film which is stabilized with a new technique developed in our group [5]. We are also studying the electronic structures of a high quality boron doped diamond film which shows a signature of the highest superconducting transition temperature of 25 K [6] and a high quality single crystal of $YbFe_2O_4$ which is one of multiferroic materials [7], by utilizing RPES at B-*K* and Fe-$M_{2,3}$ edges, respectively.

We have used the BL-5 for education activity as well, for example, practical education for undergraduate students of Okayama University. The students have an opportunity to study the synchrotron radiation mechanism and to experience XPS measurement which is very useful for the surface science research. We accepted more than 100 students from 2006 to 2012. From 2014, we have started to join the practical lecture for experiments using the beamline end stations in HiSOR for both graduate school students of Hiroshima and Okayama Universities. We have accepted 6 students in last 2 years.

REFERENCES

1. H. Okazaki *et al*., *Phys. Rev* **82**, pp. 195114 (5 pp.) (2010).
2. Y. Yoshida *et al*., *J. Phys. Soc. Jpn* **78**, pp. 034708 (4 pp.) (2009).
3. K. Saeki *et al*., *Phys. Rev* **80**, pp. 125406 (5 pp.) (2009).
4. Y. Muraoka *et al*., *MRS Proceedings* **1406** (2012).
5. Y. Muraoka *et al*., *Thin Solid Films* **599**, pp. 125-132 (2016).
6. H. Okazaki *et al*., *Appl. Phys. Lett* **106**, pp. 052601 (5 pp.) (2015).
7. K. Fujiwara *et al*., *Trans. Mater. Res. Soc. Jpn.* **41**, pp. 139-142 (2016).

X-ray photoelectron spectroscopy study of $YbCu_{1-x}Ga_x$ (x = 0.5, 1.0, 1.2, 1.5)

H. Yamaoka[a], H. Sato[b], A. Rousuli[c], N. Tsujii[d], K. Shimada[b], Y. Yamamoto[e], and J. Mizuki[e]

[a]*RIKEN SPring-8 Center, Sayo, Hyogo 679-5148, Japan*
[b]*Hiroshima Synchrotron Radiation Center, Hiroshima University, Higashi-Hiroshima, Hiroshima 739-0046, Japan*
[c]*Graduate School of Science, Hiroshima University, Higashi-Hiroshima, Hiroshima 739-0046, Japan*
[d]*Quantum Beam Center, National Institute for Materials Science, 1-2-1 Sengen, Tsukuba 305-0047, Japan*
[e]*Graduate School of Science and Technology, Kwansei Gakuin University, Sanda, Hyogo 669-1337, Japan*

Keywords: x-ray photoelectron spectroscopy, YbCuGa, valence fluctuation

Among rare-earth intermetallic compounds, Ce, Yb, and Eu have attracted much attention because of the interesting physical properties associated with the rare-earth ion valence instability. Physical properties in the valence fluctuation system could be understood by the competition between the Ruderman-Kittel-Kasuya-Yosida (RKKY) interaction and the Kondo effect, which are originated from the interaction between f and conduction electrons. When the strength of the Kondo effect is increased, the magnetic moment is screened by carrier electrons and the magnetic order is suppressed, resulting in an increase of the hybridization strength and the valence fluctuation. Temperature, pressure, and chemical substitution can change the ground state of the system.

YbCuGa is one of the Yb-based valence fluctuation systems. YbCuGa has orthorhombic $CeCu_2$-type crystal structure with space group *Imma* and Cu and Ga atoms are randomly distributed at 8c site. The thermoelectric power is negative between 20 and 300 K and also showed a broad minimum at about 190 K. Temperature dependence of the resistivity showed T^2 dependence at 4.2-90 K, showing Fermi liquid ground state.[1] X-ray absorption spectroscopy (XAS) spectra at Yb L_3 edge showed the valence fluctuation of Yb. Inelastic neutron scattering spectrum showed rather featureless response, washing out the crystal field spectrum attributed the valence fluctuation character.[2] The Kondo temperature was estimated to be about 205 K. In YbCuGa the temperature dependence of the Yb valence has not been measured so far. Recently Tsujii *et al*. synthesized polycrystalline $YbCu_{1-x}Ga_x$ (x = 0.5, 1.0, 1.2, 1.5). We have performed XAS with partial fluorescence mode (PFY-XAS) of YbCuGa, $YbCu_{0.5}Ga_{1.5}$, and $YbCu_{1.5}Ga_{0.5}$ at SPring-8. We measured the temperature and pressure dependence of the PFY-XAS spectra. These Yb compounds were valence fluctuating and the valence fluctuation of Yb is stronger in order of YbCuGa < $YbCu_{0.5}Ga_{1.5}$ < $YbCu_{1.5}Ga_{0.5}$. In the pressure dependence we found second and first order valence transitions. The temperature dependences of the Yb valence was clearly observed in YbCuGa and $YbCu_{1.5}Ga_{0.5}$, but not in $YbCu_{0.5}Ga_{1.5}$.

The valence band spectra of $YbCu_{1-x}Ga_x$ have not been measured so far. Electronic structure near the Fermi edge is also important to understand the physical properties. In this report, we briefly showed the raw data of the valence band spectra of $YbCu_{1-x}Ga_x$ measured at BL-7, HiSOR. Figure 1 shows the valence band spectra of $YbCu_{1-x}Ga_x$ (x = 0.5, 1.0, 1.2, 1.5) at low temperatures at Yb 4d-4f resonance of 182 eV. These compounds are valence fluctuating and the chemical substitution changes the Yb valence state. We measured incident energy ($h\nu$) dependence of the valence band spectra at Yb 4d-4f resonance of $YbCu_{0.5}Ga_{1.5}$ and $YbCu_{0.8}Ga_{1.2}$.

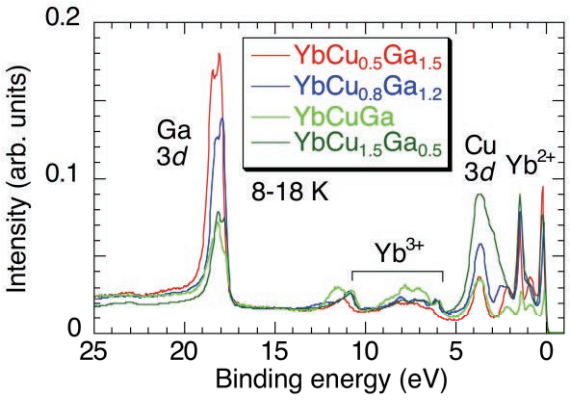

FIGURE 1. Valence band spectra of $YbCu_{1-x}Ga_x$ (x = 0.5, 1.0, 1.2, 1.5) at 8-18 K and $h\nu$ = 182 eV.

The results show a resonant energy of 182 eV, which is common in most Yb compounds.

In Fig. 2 we show the temepraturede dependence of the valence band spectra of YbCuGa and $YbCu_{1.5}Ga_{0.5}$ at $h\nu$ = 182 eV. The valence fluctuation of Yb is stronger in order of YbCuGa < $YbCu_{0.5}Ga_{1.5}$ and the result agrees with the XAS measurement. Both compounds show slight increase of the Yb valence with decreasing the temperature. This result also agrees with the XAS measurement.

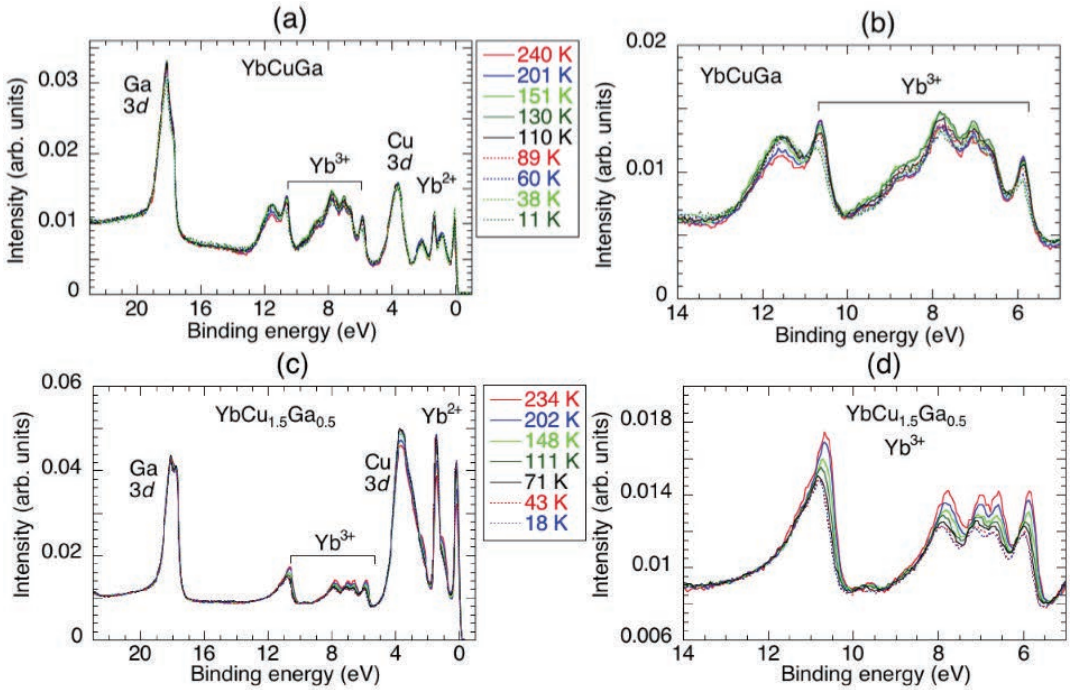

FIGURE 2. Temperature dependence of the valence band spectra of (a) YbCuGa and (c) $YbCu_{1.5}Ga_{0.5}$ at $h\nu$ = 182 eV. In (b) and (d) expanded view of the Yb^{3+} parts are shown.

References

1. D. T. Adroja, S. K. Malik, B. D. Padalia, S. N. Bhatia, R. Walia, and R. Vijayaraghavan, Phys. Rev. B **42**, 2700 (1990).
2. D.T. Adroja, B.D. Rainford, L.E. Miller, S.K. Malik, Physica. B **230-232**, 282 (1997).

15-A-35 BL-7

Angle-Resolved Photoemission Spectroscopy in Topological Crystalline Insulator $Pb_xSn_{1-x}Te$ Thin Films

Ryota Akiyama[a], Tomonari Yamaguchi[b], Di Fan[a], Yusuke Otaki[b], Hitoshi Sato[c], Akio Kimura[d], Shuji Hasegawa[a], and Shinji Kuroda[b]

[a]*The University of Tokyo, 7-3-1 Hongo, Bunkyo-ku, Tokyo, Japan*
[b]*University of Tsukuba, 1-1-1 Tennoudai, Tsukuba, Ibaraki, Japan*
[c]*Hiroshima Synchrotron Radiation Center, Hiroshima University, 2-313 Kagamiyama, Higashi-Hiroshima, Hiroshima, Japan*
[d]*Graduate School of Science, Hiroshima University, 1-3-1 Kagamiyama, Higashi Hiroshima, Hiroshima, Japan*

Keywords: topological crystalline insulator, topological insulator, spin-orbit interaction, thin film,

The two-dimensional spin-related materials attract attention much these days since they have abundant possibilities of application for next generation devices. Topological insulators (TIs) are the new class of materials which show novel properties (electrical transport, electronic structure, etc.). In three-dimensional TIs, the surface is metallic whereas the bulk is insulating. Such surface state is called topological surface state, and the spin of carriers is non-degenerated except for the Kramers degeneracy points (k = 0). The spin texture induced in the TSS is originated from the time-reversal symmetry and the band inversion by the strong spin-orbit interaction.

Topological crystalline insulators (TCIs) are the same family as TIs, but the TSS of TCIs is protected by the crystal mirror symmetry instead of the time-reversal symmetry. As the TCI material, SnTe[1], SnSe[2], $Pb_xSn_{1-x}Te$[1], $Pb_xSn_{1-x}Se$[3] have been examined and confirmed. SnTe was shown to be TCI experimentally by the angle-resolved photoemission spectroscopy (ARPES) with bulk crystals of (001) and (111) orientation in 2012 and 2013, respectively[1,4]. The electrical transport was measured in the thin films so far[5-8]. However, it is difficult to see the surface band of SnTe directly because SnTe tends to be heavily doped p-type. TSS is given by extrapolating the band near the top of the valence band. That is, the Dirac point has not been observed directly.

In this study, we aim to observe the surface band, particularly Dirac point, directly by tuning the Fermi level. If we can see the surface band around the Dirac point, we can discuss the gap opening or closing by the perturbation with doping atoms. The mechanism of the gap opening in TCI is still unknown experimentally. Therefore, it is important to check the robustness of the TSS in TCIs for understanding the intrinsic properties about TCIs. The band inversion of the valence and conduction band at L point occurs in SnTe, and it is required to realize the TSS. According to the previous reports, the band inversion of SnTe keeps with doping Pb up to x = 0.75 in the form of $Pb_xSn_{1-x}Te$. Doping of Pb make the carrier concentration low, which works good for investigating the TSS.

In this study, the samples of $Pb_xSn_{1-x}Te$(111) were made with the molecular beam epitaxy (MBE) equipment on the hybrid substrate consisting of GaAs and CdTe layer. The hybrid substrate was grown as follows. After the surface cleaning of a p-GaAs(111) substrate at 400°C by irradiating the radical hydrogen, 2 nm-ZnTe was grown on the GaAs(111) substrate at 240°C. Then, around 250 nm-CdTe(111) buffer layer was grown on it successively. At last, Te was deposited as a capping layer at around 10°C. After transferring in air to another chamber, the Te capping layer was decapped by heating at around 220°C in the ultra high vacuum environment. The $Pb_xSn_{1-x}Te$ layer was grown on it at around 250°C with using the SnTe and PbTe compound sources. The samples were transferred to the chamber for ARPES with keeping the ultra high vacuum by the homemade portable chamber.

Figures 1(a) - (c) show the band dispersion around the $\bar{\Gamma}$ point of $Pb_xSn_{1-x}Te(111)$ thin films. The incident photon energy and the Pb ratio are (a) 60 eV and x = 0, (b) 60 eV and x = 0.5, and (c) 70 eV and x = 1.0, respectively. All the samples were measured at 30 K. The valence band was seen in the all samples in the $\bar{\Gamma}$ - $\bar{K}$ scans, and the Fermi level lies inside the valence band. This indicates that the samples have the p-type degenerate semiconductor properties. The notable feature is the shifting of the Fermi level with doping Pb. The edges of the valence band are indicated by the dashed lines as a guide.

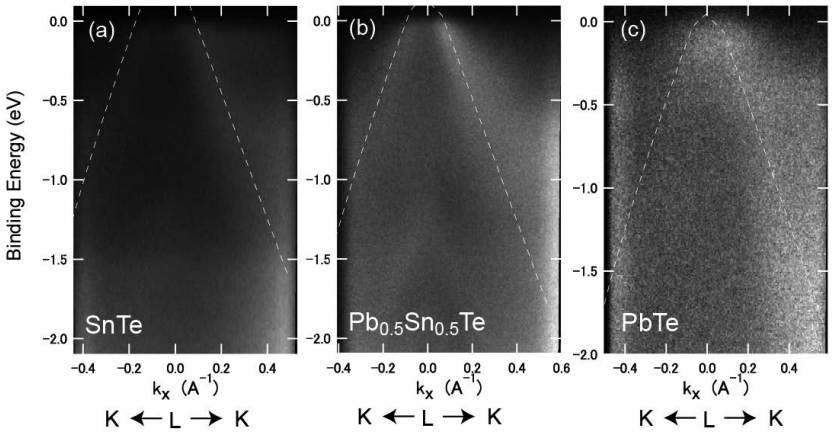

FIGURE 1. The band dispersion around $\bar{\Gamma}$ point of $Pb_xSn_{1-x}Te(111)$ thin films measured at 30 K. The incident photon energy and the Pb ratio are (a) 60 eV and x = 0, (b) 60 eV and x = 0.5, and (c) 70 eV and x = 1.0, respectively.

The band dispersion was observed also at the Γ point by changing the incident photon energy to higher energies. The Γ and L points appear alternately along the k_z direction of the three-dimensional Brillouin zone of $Pb_xSn_{1-x}Te(111)$. Because it is difficult to cleave the (111) orientation of the bulk crystal of $Pb_xSn_{1-x}Te(111)$, the band structure around Γ point has not been investigated experimentally so far. As shown in Fig. 2(a), we observed the linear-like band dispersion above the binding energy of ~ -1.5 eV in $Pb_{0.5}Sn_{0.5}Te(111)$ at the Γ point with the incident photon energy of 98 eV. The first principle calculation shows the similar band dispersion, but not the same. Such a characteristic dispersion appears after disappearing of the dispersion at L point with increasing the incident photon energy. Figure 2(b) shows the intermediate state in the transition from L (Fig. 1(a)) to Γ (Fig. 2(a)) point. Since this linear-like dispersion crosses the Fermi level the mobility of carriers are expected to be high, although the dimension of the dispersion is three because the dispersion changes its shape with changing the incident photon energy. To know the details of this dispersion, further ARPES experiments are needed as well as measuring electrical transports.

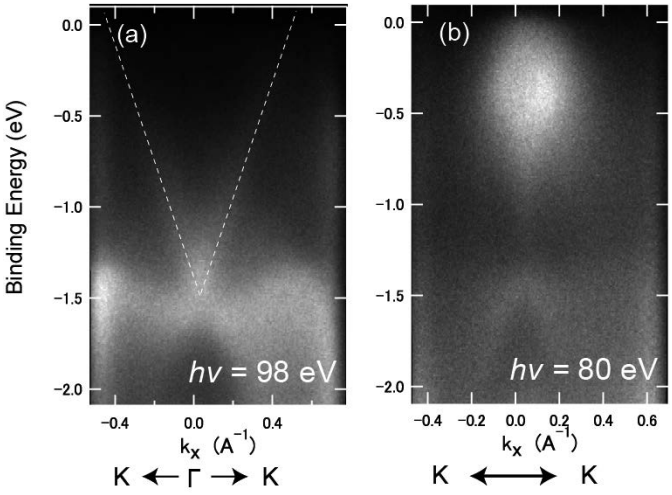

FIGURE 2. The band dispersion around Γ point of $Pb_{0.5}Sn_{0.5}Te(111)$ thin film measured at 30 K. The incident photon energy is (a) 98 and (b) 80 eV, respectively. The dashed line shown in (a) indicates the linear-like dispersion.

REFERENCES

1. Y. Tanaka, Zhi Ren, T. Sato, K. Nakayama, S. Souma *et al.*, Nat. Phys. **8**, 800 (2012).
2. Z. Wang, J. Wang, Y. Zang, Q. Zhang, J.-A. Shi *et al.*, Adv. Mater. **27**, 4150 (2015).
3. P. Dziawa, B. J. Kowalski, K. Dybko, R. Buczko, A. Szczerbakow *et al.*, Nat. Mat. **11**, 1023 (2012).
4. Y. Tanaka, T. Shoman, K. Nakayama, S. Souma, T. Sato *et al.*, Phys. Rev. B **88**, 235126 (2013).
5. A. A. Taskin, F. Yang, S. Sasaki, K. Segawa, and Y. Ando, Phys. Rev. B **89**, 121302 (2014).
6. B. A. Assaf, F. Katmis, P. Wei, B. Satpati, Z. Zhang *et al.*, Appl. Phys. Lett. **105**, 102108 (2014).
7. M. Safdar, Q. S. Wang, M. Mirza, Z. X. Wang, K. Xu, J. He, Nano Lett. **13**, 5344 (2013).
8. R. Akiyama, K. Fujisawa, T. Yamaguchi, R. Ishikawa, and S. Kuroda, Nano Research **9**, 490 (2016).

Photoemission study on electronic structure of $Yb_2Pt_6X_{15}$ (X=Al, Ga)

S. Nakamura[a], A. Rousuli[b], T. Nagasaki[b], H. Sato[c], T. Ueda[d], Y. Matsumoto[d], S. Ohara[d], K. Mimura[e], H. Anzai[e], K. Ichiki[e], S. Ueda[f], K. Shimada[c], H. Namatame[c], M. Taniguchi[c]

[a]*Faculty of Science, Hiroshima University, Higashi-Hiroshima 739-8526, Japan*
[b]*Graduate School of Science, Hiroshima University, Higashi-Hiroshima 739-8526, Japan*
[c]*Hiroshima Synchrotron Radiation Center, Hiroshima University, Higashi-Hiroshima 739-0046, Japan*
[d]*Graduate School of Engineering, Nagoya Institute of Technology, Nagoya 466-8555, Japan*
[e]*Graduate School of Engineering, Osaka Prefecture University, Sakai, Osaka 599-8531, Japan*
[f]*Synchrotron X-ray Station at SPring-8, National Institute for Materials Science, Sayo, Hyogo 679-5148, Japan*

Keywords: Yb-compounds, 4*f* electrons, *c-f* hybridization, valence fluctuation

Yb-based compounds have attracted a great interest as the strongly correlated 4*f*-electron system with the Ce-like physical phenomena such as heavy-fermion behavior, magnetic transition, valence fluctuation and unconventional superconductivity. These various properties are derived from the hybridization between 4*f* and conduction electrons (*c-f* hybridization), and are qualitatively explained by so called the Doniach phase diagram [1] with a magnetic ground state for the weak *c-f* hybridization and the Fermi liquid ground state for the strong *c-f* hybridization. Although $Yb_2Pt_6X_{15}$ (X=Ga, Al) are both the valence fluctuation compounds [2], the magnetic susceptibility of $Yb_2Pt_6Al_{15}$ with a maximum around 20 K shows the Curie-Weiss behavior above 75 K with an effective moment close to that of a free Yb^{3+} ion [3], while that of $Yb_2Pt_6Ga_{15}$ a typical behavior of valence fluctuation compounds with no maximum [2]. In terms of the Doniach phase diagram [1], $Yb_2Pt_6X_{15}$ are considered to lie on the Fermi liquid ground state region but $Yb_2Pt_6Al_{15}$ is located close to the magnetic region compared to $Yb_2Pt_6Ga_{15}$. In this study, we have investigated the electronic structure of $Yb_2Pt_6X_{15}$ by means of synchrotron radiation photoemission spectroscopy (PES) using hard x-ray ($h\nu$=5.90 keV; HAXPES) and ultraviolet region (VUVPES). HAXPES and VUVPES experiments were carried out at BL15XU of SPring-8 and BL-7 of Hiroshima Synchrotron Radiation Center (HSRC), respectively. Clean surfaces were obtained by fracturing *in situ*.

Figure 1 (a) shows the comparison of the Yb $3d_{5/2}$ HAXPES spectra of $Yb_2Pt_6X_{15}$ measured at 20 and 250 K. The single peak at 1520 eV and multiplet structures at 1525-1535 eV are derived from the Yb^{2+} and Yb^{3+}, respectively. In order to determine the Yb mean valence of $Yb_2Pt_6X_{15}$, we fitted the Yb $3d_{5/2}$ spectra using the atomic multiplet calculation for the Yb^{3+} multiplet structures. The valences are estimated to be 2.2 for $Yb_2Pt_6Ga_{15}$ and as 2.8 for $Yb_2Pt_6Al_{15}$ at 20 K from the intensity ratio of the Yb^{2+} and Yb^{3+} peaks using the $v=2+I^{3+}/(I^{2+}+I^{3+})$, where I^{2+} and I^{3+} denote the intensities of the Yb^{2+} and Yb^{3+} peaks, respectively. For $Yb_2Pt_6Al_{15}$, the valence gets closer to Yb^{2+} on cooling.

The valence-band HAXPES spectra of $Yb_2Pt_6X_{15}$ measured at 20 K are compared in Fig.1 (b). The Yb^{2+} $4f_{7/2}$ and $4f_{5/2}$ peaks exist near the Fermi energy (E_F) and 1.5 eV, respectively and the $4f_{7/2}$ peak crossing E_F indicates the valence fluctuation in consistent with the result of the Yb $3d_{5/2}$ core-level spectra. The Yb^{3+} multiplet peaks are clearly observed at 5-12 eV for $Yb_2Pt_6Al_{15}$, while almost not observed for $Yb_2Pt_6Ga_{15}$. The prominent peaks at 4-6 eV are ascribed to the Pt 5*d* state. The Pt 5*d* peak is shifted toward the lower binding-energy side on going from X=Al to Ga. The same energy shift is detected for the Pt 4*f* and $4d_{2/5}$ peaks.

Figure 2 (a) shows the Yb 4*d*-4*f* resonant PES (RPES) spectra for $Yb_2Pt_6Al_{15}$ measured at 20 K. The background contribution to the spectra has been subtracted by the Shirley's method [4]. The bulk- and surface-originated Yb^{2+} 4*f* peaks are well observed as indicated in the figure. One notices that the resonance enhancement is mostly observed for Yb^{3+} 4*f* multiplet structures at 5-12 eV at $h\nu$=180 eV near the Yb 4*d* absorption edge. Figure 2 (b) shows the RPES spectra of $Yb_2Pt_6X_{15}$ in the Yb^{3+} 4*f* region measured at $h\nu$=182 eV. Due to the resonance effect, the Yb^{3+} 4*f* multiplet peaks are clearly observed also for $Yb_2Pt_6Ga_{15}$. It is noted that Yb^{3+} 4*f* peaks are shifted toward the higher binding-energy side on going from X=Al to Ga. On the other

hand, the Pt 5*d* peak is almost not observed because $h\nu$=182 eV corresponds to the Cooper minimum for Pt 5*d*, which supports the assignment of the peaks at 4-6 eV in Fig. 1 (b) to the Pt 5*d* states.

The trends of the Yb valence and energy shifts are just similar to those observed for antiferromagnetic $YbNi_3Al_9$ and valence fluctuating compound $YbNi_3Ga_9$ [5], which suggests that the same electronic model can be applied for $Yb_2Pt_6X_{15}$. The Yb^{3+} 4*f* energy shift indicates that the Yb hole level of $Yb_2Pt_6Al_{15}$ is closer to E_F compared to $Yb_2Pt_6Ga_{15}$ and the Yb valence of $Yb_2Pt_6Ga_{15}$ gets closer to Yb^{2+}. The charge transfer from the conduction-band to Yb 4*f* states causes the energy shift of E_F in the conduction-band density of states, which is observed as the energy shifts of the Pt core states.

The *c*-*f* hybridization of $Yb_2Pt_6X_{15}$ is stronger than that of $YbNi_3X_9$. Although the Pt 5*d* states are located at the higher-binding energy compared to Ni 3*d* states, the strong *c*-*f* hybridization is qualitatively interpreted taking onto account the hybridization through the Pt 5*d* (Ni 3*d*) - X *p* hybridization.

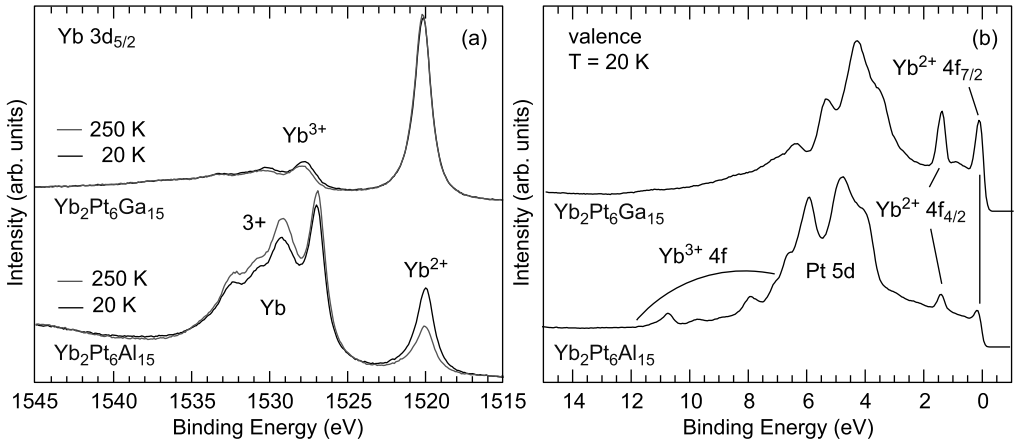

FIGURE 1. HAXPES spectra of $Yb_2Pt_6X_{15}$ for (a) Yb 3*d* and (b) valene bands.

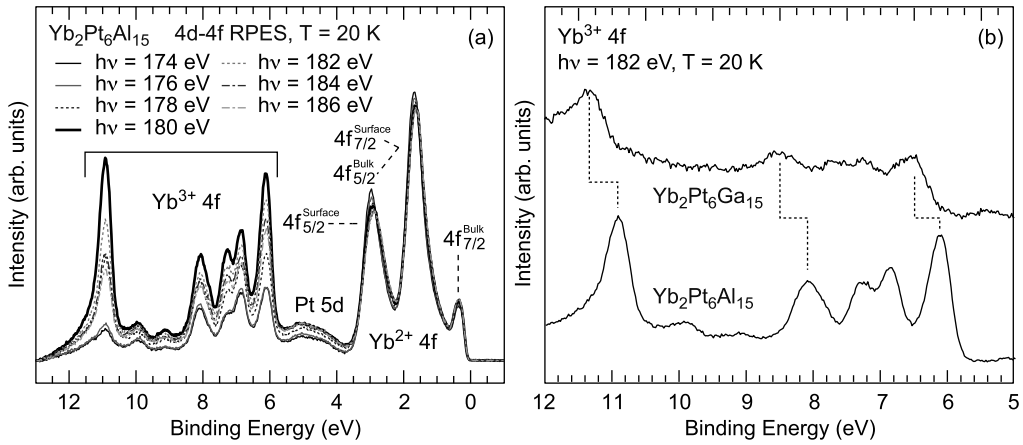

FIGURE 2. (a) Yb 4*d*-4*f* RPES spectra of $Yb_2Pt_6Al_{15}$. (b) Yb^{3+} 4*f* spectra of $Yb_2Pt_6X_{15}$ measured at $h\nu$ = 182 eV.

REFERENCES

1. S. Doniach, Physica B+C **91**, 231 (1977).
2. Y. Matsumoto *et al*., to be published in J. Phys. Conf. Series.
3. M. Deppe *et al*., New J. Phys. **10** (2008) 093017.
4. D. A. Shirley, Phys. Rev. B **5**, 4709 (1972).
5. Y. Utsumi *et al*., Phys. Rev. B **86**, 115114 (2012).

15-B-11 BL-7

Valence band structures of the layered oxychalcogenides

K. Takase[a], K. Kanno[a], S. Ishiwata[a], K. Kawamoto[a], A. Rousuli[b], T. Nagasaki[b], S. Nakamura[c], H. Sato[d], and A. Higashiya[e]

[a]*College of Science and Technology, Nihon University, Chiyoda-ku, Tokyo 101-0062, Japan*
[b]*Graduate School of Science, Hiroshima University, Kagamiyama 1-3-1, 739-8526, Japan*
[c]*Faculty of Science, Hiroshima University, Kagamiyama 1-3-1, 739-8526, Japan*
[d]*Hiroshima Synchrotron Radiation Center, Hiroshima University, Kagamiyama 2-313, 739-0046, Japan*
[e]*Faculty of Science and Engineering, Setsunan University, Neyagawa, Osaka 572-8508, Japan*

Keywords: layered oxychalcogenides, thermoelectric material, valence band structure.

The layered oxychalcogenides (LnO)CuCh (Ln=La, Bi; Ch=S, Se, Te) with the same crystal structure as the iron based superconductors, consisting of the LnO blocking layer and the CuCh conductive layer have been focused as new thermoelectric materials. Very recently, (BiO)CuSe has been reported to have relatively high figure of merit at high temperature. On the other hand, homogeneous crystal structure materials (BiO)CuTe, (LaO)CuSe, (LaO)CuTe don't indicate good thermoelectric properties. For achieving high figure of merit, large Seebeck coefficient is required. Basically, Seebeck coefficient depends on derivation of density of state against energy around Fermi energy.

In this study, the valence band structures of layered oxychalcogenides (LnO)CuCh (Ln=La, Bi; Ch=S, Se, Te) have been studied to understand the thermoelectric properties.

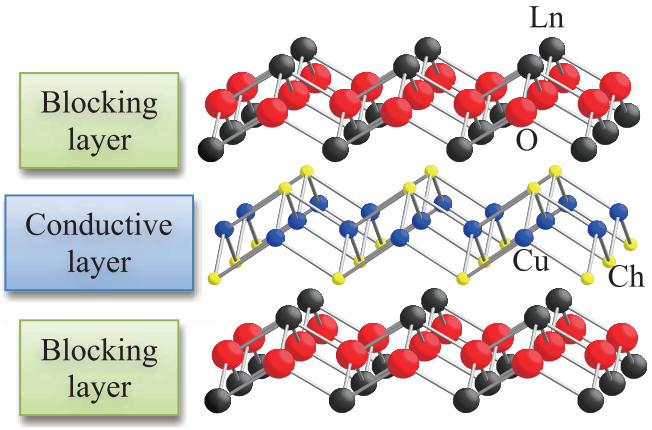

FIGURE 1. Crystal structure of the layered oxychalcogenides (LnO)CuCh (Ln=La, Bi; Ch=S, Se, Te)

All samples in this study were polycrystals prepared through solid state reaction method. Powder x-ray diffraction measurement indicated that all samples were almost single phase. From the temperature dependence of the electrical resistivity, three samples except for (BiO)CuTe were semiconductors.

Photoemission spectroscopy measurements were performed at room temperature for all samples at BL07 in HISOR with photon energy ($h\nu$) between 40 eV and 200 eV. The total resolution at $h\nu$ =200 eV, 50 eV and 40 eV were set to about 140 meV, 60 meV and 50 meV, respectively. Clean surfaces were obtained by fracturing in situ in ultrahigh vacuum of $\sim 3 \times 10^{-10}$ Torr just before the measurements.

Figure 2(a) shows the comparison of valence-band spectra obtained by $h\nu$ =200 eV for (LaO)CuSe, (LaO)CuTe, (BiO)CuSe and (BiO)CuTe. The spectral shape between Fermi level (E_F) and the binding energy (E_B) of about 2eV for Bi system is difference from those of La system. (BiO)CuSe ((BiO)CuTe) and (LaO)CuCh (Ch=Se and Te) show three structures (two structures) and a single structure in this region of E_B as indicated by vertical bars, respectively. Our experimental results suggest that substituting Bi ion for La ion influences the electronic state around E_F. On the other hand, the spectral shape of E_B between ~2 and 8 eV for (BiO)CuTe is similar to that for (LaO)CuTe and differs substantially from that of (BiO)CuSe, suggesting that this energy region is affected by the substitution of Te ion for Se ion sensitively.

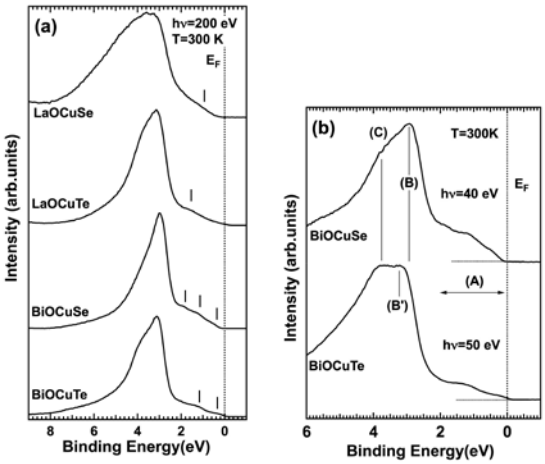

FIGURE 2. (a) Comparison of valence-band spectra obtained with $h\nu$ =200 eV at room temperature for (LaO)CuSe, (LaO)CuTe, (BiO)CuSe and (BiO)CuTe. Vertical bars indicate peak position in valence-band between E_F and E_B ~2 eV. (b) Comparison between valence-band spectrum obtained with $h\nu$ =40 eV for (BiO)CuSe and that obtained with $h\nu$ =50 eV for (BiO)CuTe. Horizontal dotted lines are zero for spectral intensity of each material. Vertical dotted line in both figures is E_F position in E_B.

Figure 2(a) shows the comparison of valence-band spectra obtained by $h\nu$ =200 eV for (LaO)CuSe, (LaO)CuTe, (BiO)CuSe and (BiO)CuTe. The spectral shape between Fermi level (E_F) and the binding energy (E_B) of about 2eV for Bi system is difference from those of La system. (BiO)CuSe ((BiO)CuTe) and (LaO)CuCh (Ch=Se and Te) show three structures (two structures) and a single structure in this region of E_B as indicated by vertical bars, respectively. Our experimental results suggest that substituting Bi ion for La ion influences the electronic state around E_F. On the other hand, the spectral shape of E_B between ~2 and 8 eV for (BiO)CuTe is similar to that for (LaO)CuTe and differs substantially from that of (BiO)CuSe, suggesting that this energy region is affected by the substitution of Te ion for Se ion sensitively.

Figure 2(b) shows comparison between a valence-band spectrum obtained with $h\nu$ =40 eV for (BiO)CuSe and that obtained with $h\nu$ =50 eV for (BiO)CuTe. From the results of band calculation using first-principles density functional theory [1], the region of (A), the peak structure around E_B=3 eV (B) and the shoulder structure around E_B=4eV (C) for (BiO)CuSe are assigned to Cu 3*d*-Se 4*p* antibonding band, Cu 3*d* non-bonding band, Cu 3*d*-Se 4*p* bonding band, respectively. Also, the results of band calculation obtained by FLAPW method using local-density approximation (LDA) for (LaO)CuSe and (LaO)CuTe demonstrate that the hybridization between Cu 3*d* and Te 5*p* states in (LaO)CuTe is stronger than that between Cu 3*d* and Se 4*p* states in (LaO)CuSe and the position of the Cu 3*d* non-bonding band in (LaO)CuTe sifts to the higher E_B side compared to that of (LaO)CuSe [2]. By taking into account the results of these band calculations, the structure of (B') and the valence-band spectrum between E_F and ~2 eV of (BiO)CuTe would correspond to Cu 3*d* non-bonding band and Cu 3*d*-Te 5*p* antibonding band, respectively.

The spectral intensity of (C) in this figure is enhanced for both materials compared to those obtained by $h\nu$ =200 eV due to the enhancement of the photoionization cross-section of Se 4*p* (Te 5*p*) orbital at $h\nu$ =40 eV (50 eV). The E_B position of (C), which corresponds to Cu 3*d*-Se 4*p* (Te 5*p*) bonding band, is same for both materials, suggesting that this band is independence from the substitution of anion (Se or Te). The (B') shifts to the higher E_B side with substituting Te ion for Se ion compared to (B) and this tendency agrees well with the calculated results of La system. Also, (BiO)CuTe has weak spectral intensity at E_F as contrasted with (BiO)CuSe, which does not have it at E_F and seems to be insulator. From the results of the band calculations, Cu 3*d*-Te 5*p* antibonding band is thought to shift to the lower E_B side compared to the Cu 3*d*-Se 4*p* antibonding band of (BiO)CuSe due to the stronger hybridization between Te 5*p* and Cu 3*d* states, where the position of the (C) structure is unchanged by the substitution of Te ion for Se ion, and consequently the weak spectral intensity at E_F may appear in (BiO)CuTe.

In order to study the electronic states near E_F in detail, we need to perform resonant photoemission spectroscopy measurement for these materials.

REFERENCES

1. S. K. Saha, *Phys. Rev.* B **92**, 041202(R) (2015).
2. K. Ueda, H. Hosono, and N. Hamada, *Journal of Applied Physics* **98** , 043506 (2005).

Metal-semiconductor transition of mineral tetrahedrite $Cu_{12}Sb_4S_{13}$ investigated by photoemission and soft x-ray absorption spectroscopies

T. Nagasaki[1], A. Rousuli[1], S. Nakamura[2], H. Sato[3], H. I. Tanaka[4], K. Suekuni[4], M. Nakatake[5], G. Kutluk[3], M. Sawada[3], K. Mimura[6], H. Anzai[6], K. Ichiki[6], S. Ueda[7], K. Shimada[3], T. Takabatake[4], H. Namatame[3] and M. Taniguchi[3]

[1]*Graduate School of Science, Hiroshima University, Higashi-Hiroshima 739-8526, Japan*
[2]*Faculty of Science, Hiroshima University, Higashi-Hiroshima 739-8526, Japan*
[3]*Hiroshima Synchrotron Radiation Center, Hiroshima University, Higashi-Hiroshima 739-0046, Japan*
[4]*AdSM, Hiroshima University, Higashi-Hiroshima 739-8530, Japan*
[5]*Aichi Synchrotron Radiation Center, Seto, Aichi 489-0965, Japan*
[6]*Graduate School of Engineering, Osaka Prefecture University, Sakai, Osaka 599-8531, Japan*
[7]*Synchrotron X-ray Station at SPring-8, National Institute for Materials Science, Sayo, Hyogo 679-5148, Japan*

Keywords: mineral tetrahedrite, metal - semiconductor transition

Mineral tetrahedrite $Cu_{12}Sb_4S_{13}$ is expected as one of candidates for environmental friendliness thermoelectric materials [1-3]. In addition, $Cu_{12}Sb_4S_{13}$ exhibits a metal - semiconductor transition (MST) at T_{MST} = 85 K [1-3]. The metallic electrical resistivity above T_{MST} sharply increases by one order of magnitude at T_{MST} and shows a semiconducting behavior below T_{MST}. The mechanism of MST is under investigation. In this study, we have investigated temperature dependence of the electronic structure of $Cu_{12}Sb_4S_{13}$ by means of synchrotron radiation photoemission spectroscopy (PES) and soft x-ray absorption spectroscopy (XAS) at the Cu $2p_{3/2}$ edge. The PES and XAS experiments were performed at BL-7 and BL-14 of Hiroshima Synchrotron Radiation Center (HSRC), respectively. We also measured hard x-ray PES (HAXPES) spectra for the Cu $2p$ core state with $h\nu$ = 5.95 keV at BL15XU of SPring-8. Clean surfaces of the polycrystalline samples were prepared by fracturing *in situ* for (HAX)PES and by scraping with a diamond file *in situ* for XAS.

Figure 1 (a) shows the PES spectra in the vicinity of the Fermi level (E_F) measured at $h\nu$ = 25 eV between 150 and 25 K. No noticeable structure is observed and we notice only a weak and broad structure in the range from 0.15 eV to E_F. The PES intensity is substantially low still in the metallic phase (T = 150 K). According to the band-structure calculation, E_F is located inside the valence bands and the band gap of 1.3 eV exists above only 0.1 eV. The low intensity well reflects this situation. With decreasing temperature, the intensity of the weak and broad structure gradually decreases though the change is relatively small above 90 K. In order to emphasize the temperature dependence of the spectra arising from the MST, we assume the background constructed from the PES spectrum at 25 K as shown by a dashed line in Fig. 1 (a) and subtract the background from each spectra. The results are shown in Fig. 1 (b) and the integrated intensities between -0.05 and 0.10 eV of the subtracted spectra are plotted as a function of temperature in Fig. 1 (c). The intensity gradually decreases on cooling and an amount of the decrease becomes steep around T_{MST}. Thus, MST is observed as the decrease of density of states (DOS) at E_F.

Figure 2 (a) shows the temperature dependence of Cu $2p_{3/2}$ XAS spectra of $Cu_{12}Sb_4S_{13}$ measured between T = 150 and 20 K. A pre-edge peak "A" at ~930.5 eV and a main peak at ~934 eV are observed at T = 150 K. The spectral feature is similar to that of monovalent copper compounds such as Cu_2O. With decreasing temperature across T_{MST}, a new feature "B" appears at ~931.5 eV between the pre-edge peak "A" and main peak. In order to emphasize the temperature dependence of the spectra observed for the peaks "A" and "B", we fit the XAS spectra using the arctan-like edge jump and three Gaussian functions as shown in Fig. 2 (a). The integrated intensities of peaks "A" and "B" are plotted as a function of temperature in Fig. 2 (b). The intensity of "A" ("B") decreases (increases) on cooling and an amount of the decrease (increase) becomes steep below T_{MST}. Since the Cu $2p$ HAXPES results indicate that Cu in $Cu_{12}Sb_4S_{13}$ is almost monovalent both in the metallic and semiconducting phases, the XAS spectra directly reflect the Cu $3d$ - derived unoccupied DOS. The reduction of

"A" intensity would reflect the decrease of DOS at E_F. The PES and XAS results suggest that DOS at E_F split away from E_F and the resultant decrease of DOS at E_F causes MST of $Cu_{12}Sb_4S_{13}$.

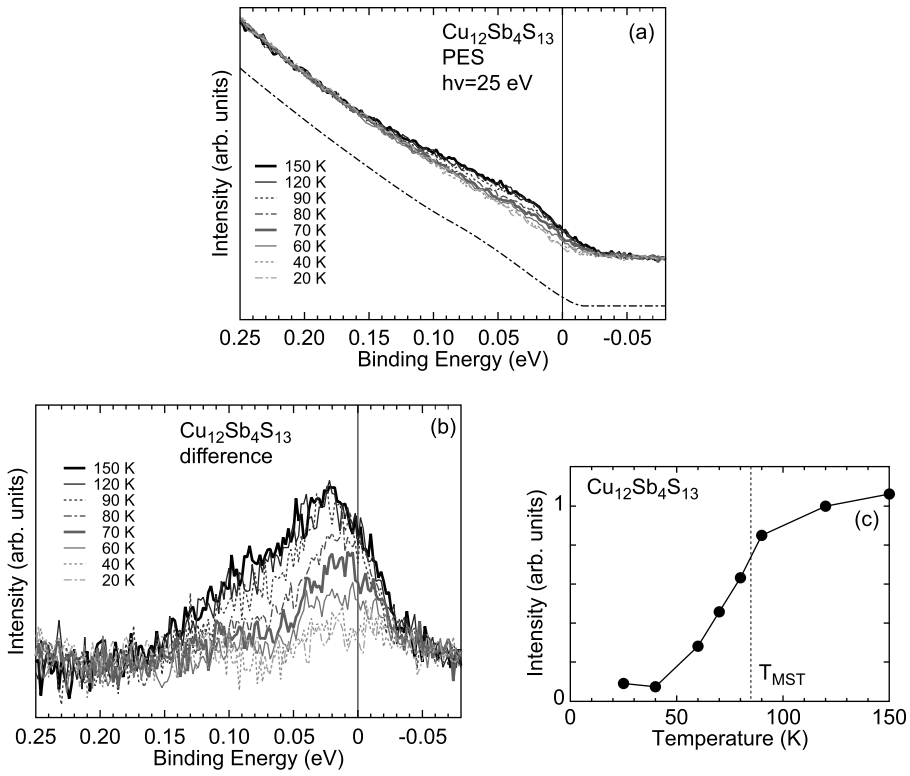

FIGURE 1. (a) Temperature dependence of PES spectra of $Cu_{12}Sb_4S_{13}$ measured at $h\nu = 25$ eV between $T = 150$ and 20 K. Dash-dotted line shows a background constructed by smoothing the spectrum at 20 K. (b) Difference spectra from background (Dash-dotted line in (a)). (c) Integrated intensity of the difference spectra between 0.10 and -0.05 eV in (b).

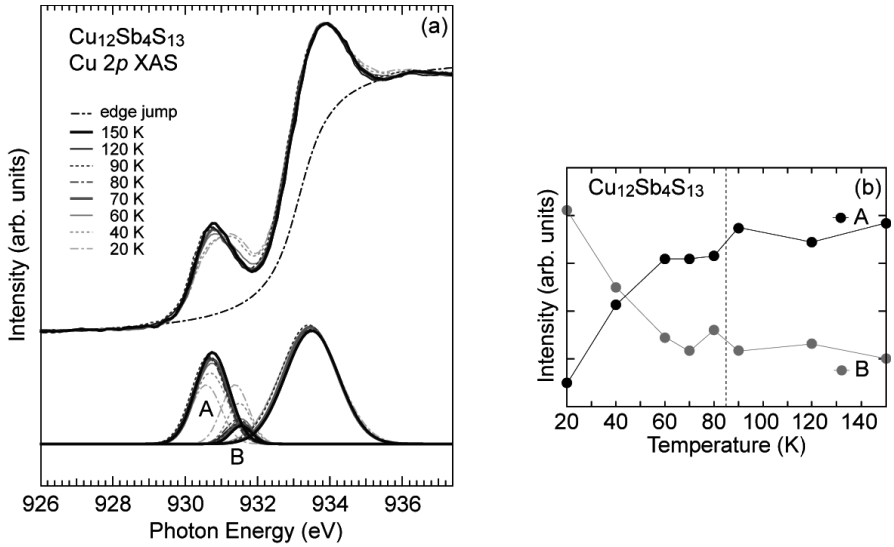

FIGURE 2. (a) Temperature dependence of Cu $2p_{3/2}$ XAS spectra of $Cu_{12}Sb_4S_{13}$ measured between $T = 150$ and 20 K together with assumed edge jump for fit (upper part) and three Gaussian functions for fit (lower part). (b) Temperature dependence of intensities of the peaks "A" and "B" in (a).

REFERENCES

1. K. Suekuni *et al*., Appl. Phys. Exp. **5**, 051201 (2012).
2. K. Suekuni *et al*., J. Appl. Phys. **113**, 043712 (2013).
3. H. I. Tanaka *et al*., J. Phys. Soc. Jpn. **85**, 014703 (2015).

Electronic States and Glass-Forming Ability of Zr-Cu-Ag Bulk Metallic Glasses

Shinya Hosokawa[a], Hidemi Kato[b], Masasi Nakatake[c], and Hitoshi Sato[d]

[a] *Department of Physics, Graduate School of Science and Technology, Kumamoto University, Kumamoto 860-8555*
[b] *Institute for Materials Research, Tohoku University, Sendai 980-8577*
[c] *Aichi Synchrotron Radiation Center, Seto 489-0965*
[d] *Hiroshima Synchrotron Radiation Center, Hiroshima University, Higashi-Hiroshima 739-0046*

Keywords: Metallic glass, Core-level, Valence band, Conduction band, Density of states

In the last two decades, bulk metallic glasses (BMG) with distinct glass transitions have been discovered in various multi-component metallic alloys. They show extremely excellent glass-forming abilities (GFA), where even a very slow cooling rate such as ~1 K/s can avoid crystallization. Physical and technological properties of these glasses were well investigated, including glass transition, structural change, phase stability, elastic constants, magnetic properties, etc [1].

Zhang et al. [2] reported that by adding Ag atoms to $Zr_{50}Cu_{50}$ alloy, their GFA greatly improves as Ag atoms to $Zr_{50}Cu_{50}$ glass, and the critical sample diameter made with Cu mold casting increases with increasing Ag content up to 6 mm at 10 at.% Ag. Since Ag has a good value of the *K* absorption energy of 25.514 keV, XAFS measurements were performed on $(Zr_{50}Cu_{50})$-Ag BMGs close to the Ag *K* edge as well as the Zr and Cu *K* edges by Fujita et al. [3]. Also, *ab initio* molecular dynamics (MD) simulations were performed on these BMGs [3], and it was concluded that an atomic-scale heterogeneity may play an important role in improving the GFA. Kawamata et al. [4] measured anomalous x-ray scattering (AXS) with reverse Monte Carlo (RMC) modeling to investigate intermediate-range local structure experimentally, and it was concluded that the improvement in the GFA appears to be associated with the local coordination around the Ag and Cu atoms.

We have also performed AXS experiments with an improved detecting system suitable for the intense third-generation synchrotron facilities, and complementary ND measurements with different weighting factors for the partial structure factors [5]. We reported short- and intermediate-range local structures evaluated from the AXS and ND data using RMC modeling.

The role of electronic structures is also helpful to understand the GFA of BMGs as was reported in Pd-Ni-Cu-P [6], Zr-Ni-Al [7], and Pd-Pt-Cu-P [8] alloys. In this project, we measured the incident-photon energy, $h\nu$, dependence of the electronic structure of the valence band by photoemission spectroscopy (PES) using synchrotron radiation, from which the Zr, Cu, and Ag partial densities of states (DOS) could be estimated.

A $Zr_{45}Cu_{45}Ag_{10}$ alloy ingot with nominal composition was prepared by arc-melting of mixtures of Zr, Ni, and Ag metals with purities of 99.5%, 99.99%, and 99.99%, respectively, in a high-purity Ar atmosphere. From this, a cylindrical rod of ~3 mm in diameter and ~10 mm in length was manufactured by tilt casting with a Cu mold. The reference $Zr_{50}Cu_{50}$ amorphous ribbon with ~0.03 mm thick and ~2 mm wide was prepared by a single roller melt-spinning technique in pure Ar atmosphere.

Figure 1 shows the incident photon energy, $h\nu$, dependence of the PES spectra of the (a) $Zr_{45}Cu_{45}Ag_{10}$ and (b) reference $Zr_{50}Cu_{50}$ metallic glasses. The data were normalized to the corresponding maximum intensities, and shown as a function of electron energy, *E,* with respect to the Fermi energy, E_F. The $h\nu$ values are indicated upper-left of each spectrum. As clearly seen in the figure, PES spectra highly depend on the $h\nu$ value. Since the photo-ionization cross-sections, σ_p, of Zr, Cu, and Ag electrons has a large $h\nu$ dependences in this $h\nu$ region, in particular the existences of Cooper minima, it is possible to obtain partial DOS using the $h\nu$ dependence of σ_p, as was performed in the $Pd_{42.5}Ni_{7.5}Cu_{30}P_{20}$ [6] and $Pd_{30}Pt_{17.5}Cu_{32.5}P_{20}$ [8] BMGs.

On the contrary, the difference of the spectra between the Ag-doped and undoped ZrCu alloys. Small differences are observed in the peak at E = –11 eV and the structure at about E = –3-4 eV, which may be originated from Ag 4*d* electrons. Detailed analyses are now in progress.

This work was performed under the inter-university cooperative research program of the Institute for Materials Research, Tohoku University (Project Nos. 14K0033 and 15K0003). The PES and IPES experiments were performed at BL7 in the HiSOR with the approval of the Hiroshima Synchrotron Radiation Center (Proposal Nos. 13-B-22 and 13-B-23).

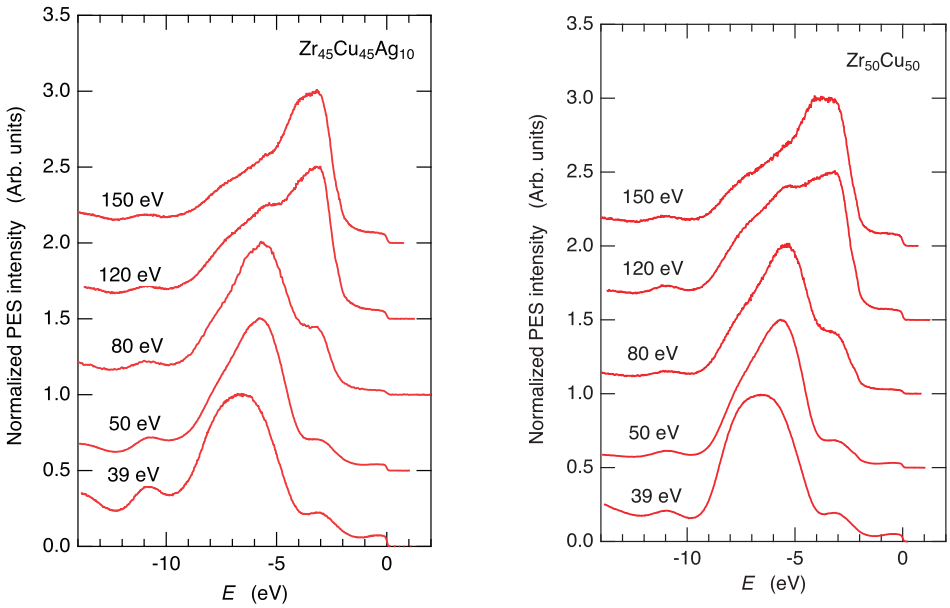

FIGURE 1. *hv* dependence of valence-band PES spectra for (a) $Zr_{45}Cu_{45}Ag_{10}$ bulk metallic glass and (b) $Zr_{50}Cu_{50}$ amorphous ribbon.

REFERENCES

1. Y. Q. Cheng and E. Ma, *Prog. Mater. Sci.* **56**, 379 (2011).
2. W. Zhang, F. Jia, Q. Zhang, and A. Inoue, *Mater. Sci. Eng. A* **459**, 330 (2007).
3. T. Fujita, K. Konno, W. Zhang, V. Kumar, M. Matsuura, A. Inoue, T. Sakurai, and M. W. Chen, *Phys. Rev. Lett.* **103**, 075502 (2009).
4. T. Kawamata, K. Sugiyama, Y. Yokoyama, and T. Fujita, *J. Phys.: Conf. Ser.* **502**, 012027 (2014).
5. S. Hosokawa, J. Stellhorn, W.-C. Pilgrim, N. Boudet, N. Blanc, S. Kohara, H. Tajiri, H. Kato, Y. Kawakita, and T. Otomo, *JPS Conf. Proc.* **8**, 031002 (2015).
6. S. Hosokawa, H. Sato, N. Happo, K. Mimura, Y. Tezuka, T. Ichitsubo, E. Matsubara, and N. Nishiyama, *Acta Mater*. **55**, 3413 (2007).
7. T. Nasu, S. Hosokawa, M. Nakatake, H. Sato, W. Zhang, and A. Inoue, *J. Phys.: Conf. Ser*. **144**, 012041 (2009).
8. S. Hosokawa, H. Sato, M. Nakatake, and N. Nishiyama, *Phys. Status Solidi B* **253**, 676 (2016).